J. Fluid Mech. (2000), *vol.* 411, *pp.* 1–38. Printed in the United Kingdom

Steady flow separation patterns in a 45 degree junction

By C. ROSS ETHIER†[1,2], SUJATA PRAKASH[1], DAVID A. STEINMAN[3], RICHARD L. LEASK[2], GREGORY G. COUCH[2] AND M. OJHA[2]

[1] Department of Mechanical and Industrial Engineering, University of Toronto, Toronto, Ontario, Canada M5S 3G8

[2] Institute for Biomedical Engineering, University of Toronto, Toronto, Ontario, Canada M5S 3G8

[3] Imaging Research Labs, Robarts Research Institute, and Department of Medical Biophysics, University of Western Ontario, London, Ontario, Canada

(Received 22 June 1999 and in revised form 22 December 1999)

Numerical and experimental techniques were used to study the physics of flow separation for steady internal flow in a 45° junction geometry, such as that observed between two pipes or between the downstream end of a bypass graft and an artery. The three-dimensional Navier–Stokes equations were solved using a validated finite element code, and complementary experiments were performed using the photochromic dye tracer technique. Inlet Reynolds numbers in the range 250 to 1650 were considered. An adaptive mesh refinement approach was adopted to ensure grid-independent solutions. Good agreement was observed between the numerical results and the experimentally measured velocity fields; however, the wall shear stress agreement was less satisfactory. Just distal to the 'toe' of the junction, axial flow separation was observed for all Reynolds numbers greater than 250. Further downstream (approximately 1.3 diameters from the toe), the axial flow again separated for $Re \geqslant 450$. The location and structure of axial flow separation in this geometry is controlled by secondary flows, which at sufficiently high *Re* create free stagnation points on the model symmetry plane. In fact, separation in this flow is best explained by a secondary flow boundary layer collision model, analogous to that proposed for flow in the entry region of a curved tube. Novel features of this flow include axial flow separation at modest *Re* (as compared to flow in a curved tube, where separation occurs only at much higher *Re*), and the existence and interaction of two distinct three-dimensional separation zones.

1. Introduction

Understanding flow separation is of particular importance, since it affects numerous physical processes, such as pressure and energy loss, heat and mass transfer, and vortex shedding. Additionally, the development of several types of arterial disease has been postulated to depend on blood flow separation patterns and their effects on the arterial wall (Nerem & Cornhill 1980; Ojha 1993). The definition of 'separation' in a fully three-dimensional flow is more complex than in the two-dimensional situation. It is best understood by looking at singular points in the so-called 'limiting streamline' field (also called 'wall streamlines' or 'skin friction lines'; see e.g. Tobak & Peake 1982).

† Author to whom correspondence should be addressed: e-mail: ethier@mie.utoronto.ca.

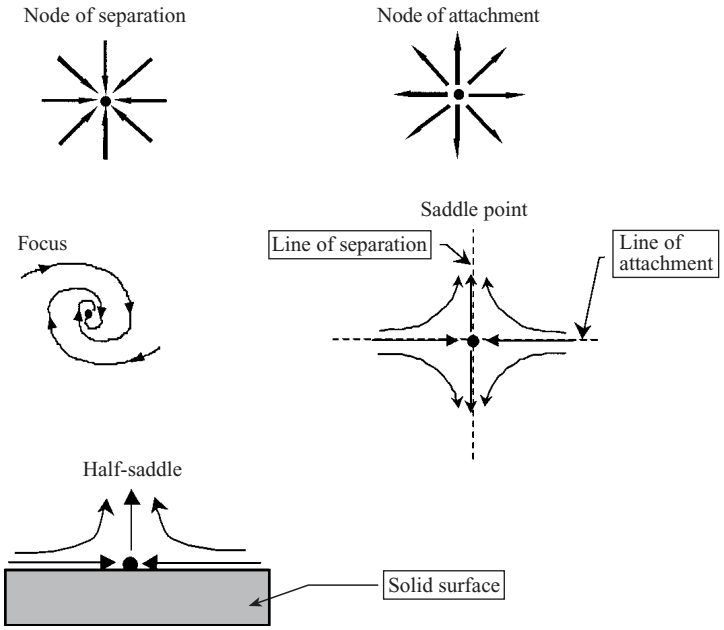

FIGURE 1. Schematic description of streamline topology in the neighbourhood of critical points. Singular points can be defined by the limiting wall shear stress field on solid surfaces, or by streamlines on a surface cutting the flow. The terms 'node of separation', 'node of attachment', 'line of attachment' and 'line of separation' are only valid for the case of singular points defined by a limiting wall shear stress field on a solid surface. More specifically, in the case of the saddle, the limiting streamlines onto which all other limiting streamlines converge define the line of separation; the limiting streamlines from which all others diverge define the line of attachment. Not immediately evident from this schematic is the three-dimensional nature of the flow in the neighbourhood of critical points. For example, consider a cutting surface oriented perpendicularly to a solid surface bounding the flow. If the cutting surface passes though a node of attachment, a half-saddle streamline pattern is obtained on the cutting surface. If it passes through a line of separation, a half-nodal pattern is obtained on the cutting surface, etc.

The limiting streamlines are interpreted as trajectories arising from the vector-valued wall shear stress field on the solid surface. Singular points in the limiting streamline field, defined as those points at which both components of the shear stress vanish, can be divided into two main classes: saddle points and nodes; nodes can be further subclassified into nodal points and foci (Hunt *et al.* 1978; Tobak & Peake 1982) (figure 1). Following Tobak & Peake (1982), we define three-dimensional separation as the phenomenon occurring when limiting streamlines converge onto a particular limiting streamline emanating from a saddle point. The limiting streamline onto which multiple streamlines converge is the *line of separation.*

In many flows, separation is three-dimensional and unsteady, with the size and structure of the separation zone(s) demonstrating a strong Reynolds number (Re) dependence. For example, Armaly *et al.* (1983), in their study of flow through an asymmetric expansion in a rectangular channel, observed two separation vortices at low Re: the first vortex was associated with the primary separation region, while the second was localized on the wall opposite the step. At low Re, the size of these separation regions increased with Re. However, with the onset of unsteadiness at higher Re, the time-averaged data demonstrated a third vortex on the same wall as

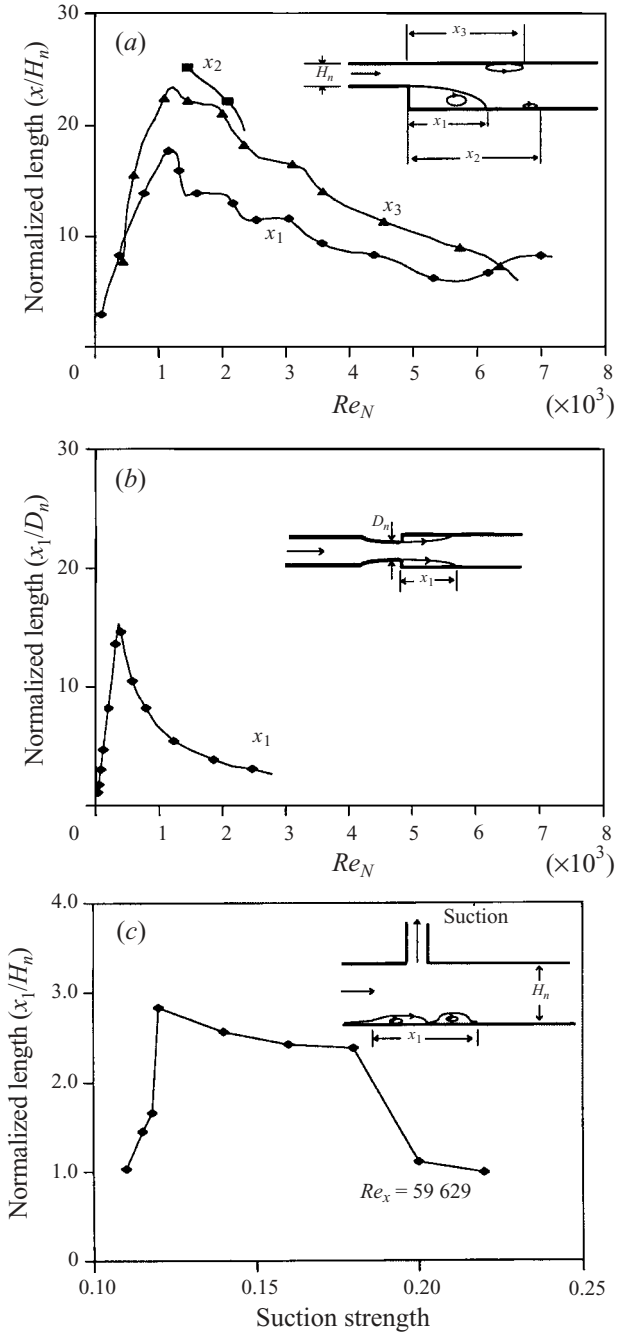

FIGURE 2. Summary of the locations of separation regions as a function of either Reynolds number or suction strength from various studies. (*a*) Flow through an asymmetric expansion in a rectangular channel (based on Armaly *et al.* 1983). (*b*) An axisymmetric expansion in a circular pipe (based on Iribarne *et al.* 1972). (*c*) A rectangular channel with suction from a side branch (based on Pauley *et al.* 1990). Re_N is nozzle Reynolds number obtained from the constricted section of the tube/channel; Re_x is based on the distance from the channel entry to the start of the suction port (x) and the velocity at the channel entrance in the absence of suction effects.

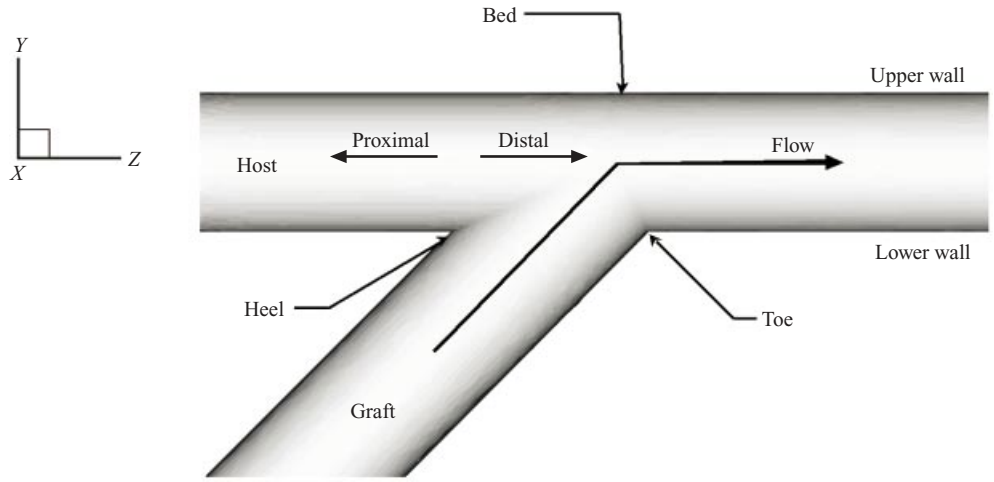

FIGURE 3. Schematic description of the graft–host junction geometry considered in the present work. The Z-axis corresponds to the centreline of the host tube, with the $Z = 0$ plane passing through the toe.

the primary separation zone. Further, the lengths of the separation zones decreased rapidly with onset of unsteadiness (figure 2*a*). Studies of flow through a symmetric expansion in a circular tube show a similar gradual growth of the separation zone length with *Re*, followed by a rapid decrease associated with the onset of unsteadiness (figure 2*b*). These observations are generally consistent with those of Armaly *et al.*, despite the fact that in the circular tube case a relatively constant flow separation length around the circumference of the tube was observed, even under unsteady conditions where the instantaneous velocity distribution was asymmetric (Iribarne *et al.* 1972; Ojha *et al.* 1989, 1990).

Several recent studies have examined in detail unsteady features during the development of two-dimensional (Pauley, Moin & Reynolds 1990) and three-dimensional separation in internal flow (Henk & Reed 1993; Pauley 1994). In the case of suction flow through a side-branch from a rectangular channel, the separation structure on the floor of the channel in the symmetry plane was the typical classical separation bubble at low *Re* (Pauley *et al.* 1990). However, with the onset of unsteadiness and vortex shedding, an unstable multiple vortex structure was produced which consisted of two co-rotating vortices separated by a relatively small region of counter-rotating fluid (figure 2*c*). When the instantaneous streamlines were time-averaged, the structure appeared as a single separation bubble with a very small region of counter-rotating fluid lying in the central region of the bubble.

Summarizing the above, single separation zones typically exist at low *Re* (order tens to hundreds) in internal flows. For both steady (Armaly *et al.* 1983; Iribarne *et al.* 1972; Macagno & Hung 1967; Pauley *et al.* 1990) and pulsatile (Ojha *et al.* 1989) flow, as the Reynolds number or adverse pressure gradient is increased, the size of the separation zone increases. With further increase in the Reynolds number or adverse pressure gradient, unsteadiness is initiated, as characterized by roll-up and/or oscillation of the shear layer and vortex shedding. Coincident with the development of unsteadiness, the length of the separation region decreases.

In the present work we have studied separation in internal flow through a model consisting of two cylindrical tubes of equal diameter joining at a 45° angle (figure 3).

This geometry is relevant in studies of flow in the cardiovascular system, where it is known as an end-to-side anastomosis between a bypass graft and a host artery, and more generally can be considered a prototype for a generic junction between two pipes. Experiments indicated the existence of a complex separation pattern in this flow; however, the features of the separation process differed in important ways from those described above. Since a complete experimental description of three-dimensional flow patterns in this geometry was not available, fundamental understanding of the physics underlying the separation processes was lacking. To better elucidate the separation flow structures, complementary computational work was therefore undertaken. The goal of this paper is to describe the major features of flow separation in a 45° junction geometry, with emphasis on the important role of secondary flows.

2. Methods

2.1. *Experimental techniques*

The model used for experimental studies was a block of ultraviolet-transparent Plexiglas (refractive index = 1.49) containing two carefully machined right cylindrical channels of internal diameter 10 mm joining at 45°. The proximal portion of the so-called host tube (see figure 3 for terminology) was occluded 3 cm proximal to the heel, and the inlet section was sufficiently long (96 diameters) to ensure fully developed flow entering the test section. The test fluid was kerosene (Shell-Sol 715; $\rho = 0.755\,\mathrm{g\,ml^{-1}}$; $\mu = 1.43$ cP at 20 °C; refractive index = 1.43) to which 0.007% by weight of the photochromic dye 1′, 3′, 3′-trimethylindoline-6-nitro-benzospiropyran was added. Upon exposure to ultraviolet light, this solution becomes dark blue in less than 1 μs, allowing dye lines to be formed non-invasively in a test section by appropriate irradiation with a collimated ultraviolet beam (Ojha *et al.* 1989).

In the first phase of the study, steady flow in the model was obtained using a computer-controlled piston pump (UHDC, London, Ontario) at a variety of flow rates, leading to Reynolds numbers (based on mean inlet velocity and tube diameter) of 275 to 1650. Clearly noticeable velocity transients lasting for approximately 2 s in the entrance region and downstream of the toe of the junction were created during turn-around of the piston in the pump. Any traces gathered during this turn-around transient were unambiguously distinguishable from other traces and were manually discarded. Multiple dye lines were simultaneously formed on the symmetry plane of the model using a XeF excimer laser (LSI Laser Sciences, St. Laurent, Quebec) and a lens array comprising 22 segments, arranged so that the inter-trace spacing was 1 mm. Traces were photographed on 35 mm film (Kodak Technical Pan 2415 film) 10 to 20 ms following trace formation. Each photographic frame was digitized with a Nikon LS3500 film scanner using a resolution of 3072×2048 pixels with 256 grey levels. Analysis of the displacement of the dye lines allowed flow patterns in the symmetry plane to be deduced. In particular, wall shear rate was obtained from dye trace profiles within 0.2 mm of the vessel wall by fitting a third-order polynomial through approximately eight points in this region. Further details of the technique, including its accuracy for wall shear stress estimation, are provided elsewhere (Ojha *et al.* 1988, 1989).

In the second phase of the study, more detailed measurements were undertaken for steady flow at a Reynolds number of 550. The experimental apparatus and methodology have been described in detail by Couch and co-workers (Couch, Johnston & Ojha 1996; Couch, Kim & Ojha 1997), and will be only briefly reviewed here. The

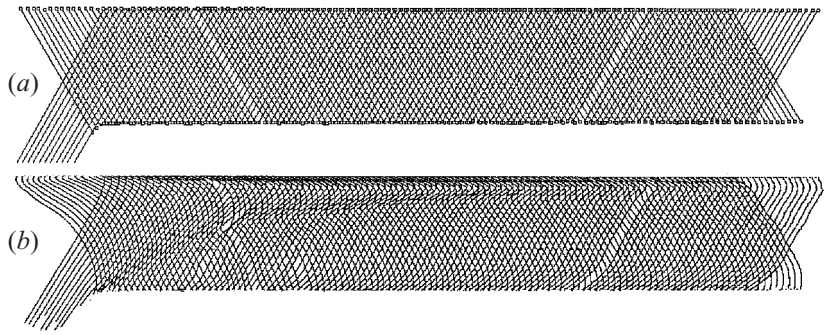

FIGURE 4. Photochromic grids. (*a*) The 'undisplaced' grid was produced from individual traces captured immediately after the laser was pulsed. (*b*) Displaced traces were imaged 10 ms after laser activation. Each displaced trace represents an average of five trace images. The grid spacing was 0.5 mm. Spaces in the photochromic grid correspond to erroneous traces that were manually removed.

methodology relies on the formation of a 'photochromic grid', obtained by firing a single laser beam at multiple locations and angles across the test section. This was accomplished by mounting the test section on a traversing stage, and moving it with respect to the laser beam so that the entire region of interest in the test section was sampled. In more detail, for each position of the test section, the following steps were taken.

1. An individual photochromic dye line was formed at an angle to the host tube axis by firing a UV laser (VSL 337ND-10Hz, Laser Science Inc., Newton, MA). A 'subtraction image' of this dye line was obtained 0 ms after firing the laser.†
2. The subtraction image of step 1 was digitally processed to extract the dye line, which was then stored as the 'undisplaced trace'.
3. Step 1 was repeated five times to obtain five individual subtraction images. In each of these images the time delay between laser firing and image acquisition was 10 ms.
4. The five images obtained in step 3 were averaged pixel-wise, and the averaged image was digitally processed to extract the dye line. This dye line was recorded as the 'displaced trace'.

The model was then moved to the next grid position (0.5 ± 0.01 mm displacement) and the entire process was repeated. After traversing the measurement region of the test section, the above procedure was repeated using a different angle between the host tube and the laser beam. The new angle was selected so that traces obtained with the second angle would be approximately perpendicular to the traces created with the first angle.

By overlaying the traces obtained in this manner, 'undisplaced' and 'displaced' photochromic grids were created (figure 4). Fluid displacement field vectors in the imaging plane were obtained by mapping the intersections of the undisplaced traces

† Acquiring each 'subtraction image' was a three-step process. First, a background image of the model was acquired with a CCD camera (Kodak MegaPlus 1400, Eastman Kodak, San Diego, CA) and image-processing board (Dipix XPG 1000, Ottawa Ontario), and stored in a temporary buffer on the imaging board. Second, the laser was fired, and after a time delay of either 0 or 10 ms, an image of the model containing the photochromic dye trace was acquired. Third, the background image was subtracted from the trace-containing image, thereby yielding the subtraction image.

to the corresponding displaced trace intersections. Approximations to the local fluid velocity in the imaging plane were then obtained by dividing the fluid displacement vector by the 10 ms delay time. Occasionally, clearly erroneous traces were produced when the pump piston reached the end of its travel and reversed. These traces were manually removed.

This procedure was carried out on 10 different measuring planes in the model. Specifically, parallel to the (Y,Z)-plane (i.e. parallel to the symmetry plane of the model; see figure 3), data were acquired on the $X = 0$, $\pm 0.3R$, and $\pm 0.5R$ planes, where R is the host tube radius. Parallel to the (X,Z)-plane, data were acquired on the $Y = -0.6R$, $-0.4R$, $-0.1R$, $0.3R$ and $0.5R$ planes. For each imaging plane the optics were adjusted as much as possible so that traces were parallel to the imaging plane, as judged by a sharp trace appearance across the entire field of view. This was important for imaging planes other than the $X = 0$ and $Y = 0$ planes, due to refractive index differences between the model and working fluid and the circular cross-section of the host tube.

2.2. *Numerical techniques*

The unsteady, incompressible, three-dimensional Navier–Stokes equations without body force terms were solved in Cartesian coordinates using a finite-element-based code. Newtonian fluid behaviour and rigid walls were assumed. The numerical approach is described in detail in Ethier, Steinman & Ojha (1999) and Minev & Ethier (1998), and is briefly summarized here. After non-dimensionalization of all velocities by the mean inlet velocity U, of all spatial positions by the graft tube diameter D, of all stresses by ρU^2, and of time by the inverse of a circular frequency ω^{-1}, the governing equations are

$$\frac{4\alpha^2}{\mathrm{Re}}\frac{\partial \boldsymbol{u}}{\partial t} + \boldsymbol{u}\cdot\nabla\boldsymbol{u} = -\nabla p + \frac{1}{\mathrm{Re}}\nabla^2\boldsymbol{u}, \tag{1}$$

$$\nabla\cdot\boldsymbol{u} = 0, \tag{2}$$

where $\alpha = D/2\sqrt{\omega/v}$ is the Womersley parameter, and $Re = UD/v$ is the Reynolds number. The convective terms were decoupled from the unsteady Stokes equations using a second-order operator-integration-factor time-splitting approach for continuous systems, based on the work of Maday, Patera & Rønquist (1990) for discrete systems. The resulting temporally discretized equations were

$$\frac{4\alpha^2}{\mathrm{Re}}\left(\frac{3\boldsymbol{u}^{n+1} - 4\tilde{\boldsymbol{u}}^{n} + \tilde{\boldsymbol{u}}^{n-1}}{2\Delta t}\right) = -\nabla p^{n+1} + \frac{1}{\mathrm{Re}}\nabla^2\boldsymbol{u}^{n+1}, \tag{3}$$

$$\nabla\cdot\boldsymbol{u}^{n+1} = 0. \tag{4}$$

Here $\boldsymbol{u}^{n+1}$ and p^{n+1} are the (semi-discrete) velocity and pressure at time level $n+1$, while $\tilde{\boldsymbol{u}}^{n-i}\,(i = 0,1)$ is a 'convected' velocity field at time level $n+1$ obtained by integrating the pure advection equation between time levels $(n-i)\Delta t$ and $(n+1)\Delta t$ (Maday *et al.* 1990). The $\tilde{\boldsymbol{u}}$ appearing in equation (3) were determined by a 'direct' Lagrangian integration of the pure advection equation, as described in detail by Minev & Ethier (1998). Briefly, this involved integration of an extrapolated velocity field to determine characteristic lines terminating at the nodal points of the Eulerian finite element mesh at time level $n+1$, followed by projection of field information along these characteristics.

Equations (3) and (4) were spatially discretized using a Galerkin finite element

approach, leading to

$$\left(\frac{3}{2\Delta t}\boldsymbol{M}+\boldsymbol{S}\right)\{u_i\}^{n+1}+\mathrm{Re}\,\boldsymbol{L}_i^T\{p\}^{n+1}$$

$$=\boldsymbol{M}\left(\frac{4\{\tilde{u}_i\}^n-\{\tilde{u}_i\}^{n-1}}{2\Delta t}\right)+\{\text{boundary terms}_i\}, \tag{5}$$

$$\sum_{i=1}^{3}\boldsymbol{L}_i\{u_i\}^{n+1}=0, \tag{6}$$

where $\{p\}$, $\{\tilde{u}_i\}$ and $\{u_i\}$ are global vectors of nodal values; $\boldsymbol{M}$, $\boldsymbol{S}$, and $\boldsymbol{L}_i$ are the consistent mass, diffusion, and divergence matrices, respectively; and ^{T} denotes transpose. Entries in the above matrices are

$$\boldsymbol{M}_{kl}=4\alpha^2\int_\Omega\phi_k\phi_l\,\mathrm{d}\Omega, \tag{7}$$

$$\boldsymbol{S}_{kl}=\int_\Omega\nabla\phi_k\cdot\nabla\phi_l\,\mathrm{d}\Omega, \tag{8}$$

$$\boldsymbol{L}_{ikl}=-\int_\Omega\psi_k\frac{\partial\phi_l}{\partial x_i}\,\mathrm{d}\Omega, \tag{9}$$

where ϕ_k and ψ_k are the (global) velocity and pressure shape functions on the computational domain Ω. The kth component of the boundary terms in equation (5) is given by

$$\{\text{boundary terms}_i\}_k=\int_\Gamma\phi_k\left(-\mathrm{Re}\,p^{n+1}\hat{\boldsymbol{n}}\cdot\hat{\boldsymbol{x}}_i+\frac{\partial u_i^{n+1}}{\partial n}\right)\mathrm{d}\Gamma, \tag{10}$$

where Γ is the boundary of Ω, $\hat{\boldsymbol{n}}$ is the unit normal to Γ, and $\hat{\boldsymbol{x}}_i$ is the unit vector in the x_i-direction. In practice the integral in equation (10) is evaluated only on regions of the boundary where there is a Neumann (outflow) condition for u_i; in regions with Dirichlet conditions, the kth component of u_i is condensed from the linear system and thus the integral in (10) does not need to be formed. Elemental matrices were formed by Gaussian quadrature using the formulas given by Keast (1986) with 15 Gauss points per tetrahedral element.

At every time step the $\{\tilde{u}_i\}$ on the right-hand side of equation (5) were computed, and then equations (5) and (6) were solved using a preconditioned conjugate gradient Uzawa method (Cahouet & Chabard 1988). Isoparametric P2–P1 Taylor–Hood tetrahedral elements (10 velocity nodes, 4 pressure nodes) satisfying the LBB condition (Glowinski & Pironneau 1992) were used. This code, and an earlier version, has been extensively validated (Ethier *et al.* 1999; Minev & Ethier 1998; Steinman *et al.* 1996) against experimental data (Ethier *et al.* 1999) and an analytical solution (Ethier & Steinman 1994). For Courant numbers of order one, the computational algorithm exhibits a velocity error which is of $O(h^3, \Delta t^2)$, where h is a characteristic mesh spacing.

2.2.1. *Finite element meshing and solution strategy*

All simulations were carried out in a half-model of the junction exploiting the symmetry of the original geometry. The inlet and outlet lengths were 6 diameters and 18 diameters, respectively. By varying the outlet length of the model, it was

confirmed that an outlet length of 18 diameters was sufficient to ensure that outlet boundary condition did not affect flow features in the region of interest near the toe. A fully developed (Poiseuille) velocity profile was specified at the graft tube inlet, the no-slip condition was applied at all solid walls, a traction-free condition was imposed at the outlet, and a symmetry condition was applied on the centreplane. For purposes of obtaining steady solutions, time-marching to steady state was employed ($||\mathrm{d}u/\mathrm{d}t||_{L_2} \leqslant 10^{-4}$). For steady problems, the frequency ω is arbitrary, and was selected to give maximum convergence rate while maintaining stability. Streamlines were computed in a post-processing step using the Tecplot visualization package (v. 7.5; Amtec Engineering, Bellevue, WA), which employs an adaptive predictor–corrector algorithm. Wall shear stresses were computed in a post-processing step by analytic differentiation of the velocity shape functions, as described in detail elsewhere (Ethier *et al.* 1999). The formal spatial accuracy of the wall shear stress field is therefore one order lower than that of the velocity field.

In an initial study, we used the P-cube and T-grid meshing packages (Fluent Inc., Lebanon, NH) to generate a series of finite element meshes of increasing density, beginning with 19 907 elements (31 056 nodes) and ending with 88 425 elements (139 617 nodes). However, even at the highest mesh density, some wall shear stress features in the separation region showed weak mesh dependence. To ensure fully mesh-independent velocity and wall shear stress fields, we therefore repeated the simulations using an adaptively refined series of meshes. The complete adaptive mesh refinement procedure is described in detail elsewhere (Prakash 1999; Prakash & Ethier 1999, 2000); here we summarize the main features.

After computation of an initial solution at $Re_D = 550$ on a coarse mesh of 3080 elements, the elemental errors were estimated using an extension of the Zienkiewicz and Zhu (Z^2) gradient recovery technique (Zienkiewicz & Zhu 1992). In this technique, a smooth velocity gradient field is 'recovered' from the computed field by minimizing the square of the difference between the recovered velocity gradient field and the finite element velocity gradient field over a local element patch. This recovered velocity gradient field is then compared to the finite element gradient to estimate the solution error. We modified the Z^2 local patch recovery method by adding the integral of the square of the residual of the continuity equation to the original recovery functional so as to enforce the continuity constraint in the recovered velocity gradient field. Specifically, we minimized the following enhanced functional:

$$F(\sigma^*)_{enhanced} = \int_{\Omega_p} (\sigma^* - \hat{\sigma})^2 \, \mathrm{d}\Omega + \int_{\Omega_p} (\sigma^*_{xx} + \sigma^*_{yy} + \sigma^*_{zz})^2 \, \mathrm{d}\Omega \tag{11}$$

where Ω_p is the domain of the element patch, $\hat{\sigma}$ is the velocity gradient derived from the finite element solution, and σ^* is the recovered velocity gradient. With the recovered gradients available, the L_2 norm of the rate-of-strain error for an element was then defined as

$$||\bar{e}_2||_i^2 = \int_{\Omega_i} \left\{ (\sigma^*_{xx} - \hat{\sigma}_{xx})^2 + (\sigma^*_{yy} - \hat{\sigma}_{yy})^2 + (\sigma^*_{zz} - \hat{\sigma}_{zz})^2 + 2(\sigma^*_{xy} - \hat{\sigma}_{xy})^2 \right.$$
$$\left. + 2(\sigma^*_{xz} - \hat{\sigma}_{xz})^2 + 2(\sigma^*_{yz} - \hat{\sigma}_{yz})^2 \right\} \mathrm{d}\Omega_i, \tag{12}$$

where Ω_i denotes the ith element.

After estimation of the elemental errors, a refinement index (Prakash *et al.* 1999) was computed for every element in the mesh, and was used to tag elements for refinement. The mesh was then refined using an extension of the octasection algorithm (Liu & Joe

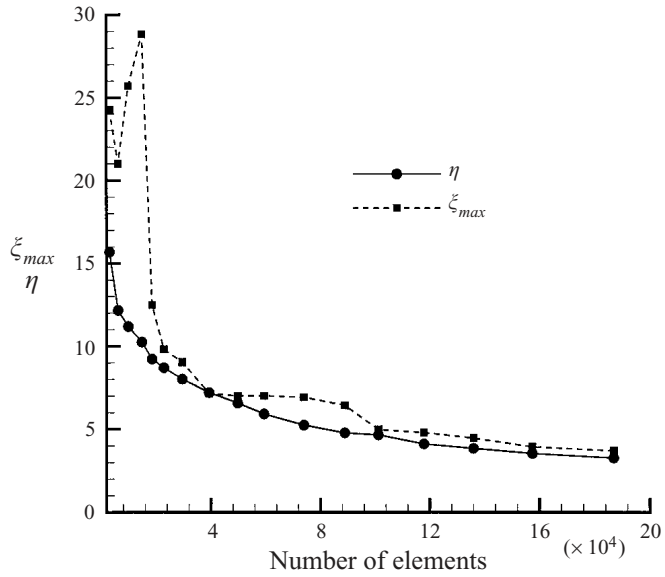

FIGURE 5. Variation of the global percentage relative error, η, and the maximum element refinement index, ξ_{max}, in the mesh as a function of mesh size for $Re_D = 550$. The global percentage relative error is the estimated overall error in the computational domain. ξ_{max} is the maximum value of the element refinement indicator for all elements in the mesh (Zienkiewicz & Zhu 1992). Larger values of ξ_{max} typically indicate unequal error distributions between elements, and the need for mesh refinement.

1996) for 10-noded tetrahedral elements. This procedure was continued until effective mesh independence had been attained, as judged by the following three criteria. First, the estimated global relative error and the maximum element refinement index were tracked (figure 5) until evidence of asymptotic convergence of these parameters was observed. Second, extracted velocity profiles at different axial locations for different meshes were compared until they showed effective mesh independence. Third, wall shear stress patterns were compared for different meshes until they showed effective mesh independence. This last criterion was by far the most sensitive, i.e. refinement of a moderately resolved mesh frequently produced appreciable changes in wall shear stress with little detectable change in velocity profiles. In fact, we found that the most sensitive way to detect mesh dependence was to plot contours of zero axial wall shear stress for different mesh densities. Our results (figure 6) show an essentially mesh-independent solution for such contours. As well, the locations of critical points in the wall shear stress field showed effective mesh independence, as will be discussed in § 3.3.

In total, 16 generations of refinement were carried out, with the final mesh in the adaptive process containing 186 970 elements (271 530 nodes per half-geometry). The minimum, maximum and average inter-nodal distances for this finest mesh were 0.0015, 0.57 and 0.0454 diameters, respectively. Refinement was clustered along a spiral path on the sidewall (figure 7), which, as will be seen, corresponds to the helical path of high-momentum fluid as it spirals down the host tube after impacting on the bed of the host tube. The 186 970 element mesh was used for simulations at $Re_D = 400$, 550 and 700, which are the primary Re of interest in this work. Somewhat

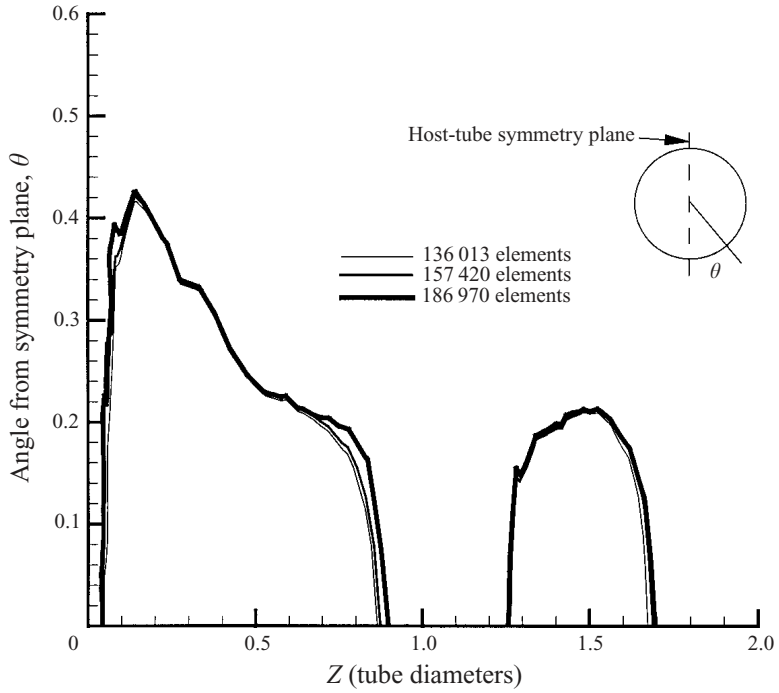

FIGURE 6. Plot showing dependence of zero axial wall shear stress contours on mesh density in host tube at $Re_D = 550$. The three densest meshes of the refined series are shown for half of the geometry. θ is defined to be the angular position of a point on the wall, measured with respect to the symmetry plane of the model, as shown in the inset.

coarser meshes were used for simulations at other Re_D of 350, 450, 500, 600, 825, and 1000, and results at these Re are only briefly mentioned.

3. Results

3.1. *Overview and numerical/experimental comparison*

Based on experimental data and numerical results, the following general features of the velocity field can be identified:

1. A core of high-momentum fluid enters the junction from the graft tube and travels towards a stagnation point on the bed of the host tube. In the neighbourhood of this stagnation point, the flow splits into forward and retrograde components having large near-wall velocities (figure 8 and figure 9). This results in zones of high shear stress around the stagnation point.

2. The proximal portion of the host tube shows weak counter-rotating vortices on the symmetry plane. For Re in the range 400–700, two such vortices are present. The exact locations and strengths of the vortices in this region are only weakly dependent on Re.

3. Extremely strong secondary flows are present in the downstream section of the host tube, qualitatively similar to Dean-type vortices (figure 10). The magnitude of the secondary flows increases with increasing Re, leading to a tighter pitch of the helical fluid paths within the host tube. The magnitude of the secondary velocity associated with this motion is quite large; for example, at $Re = 550$, the

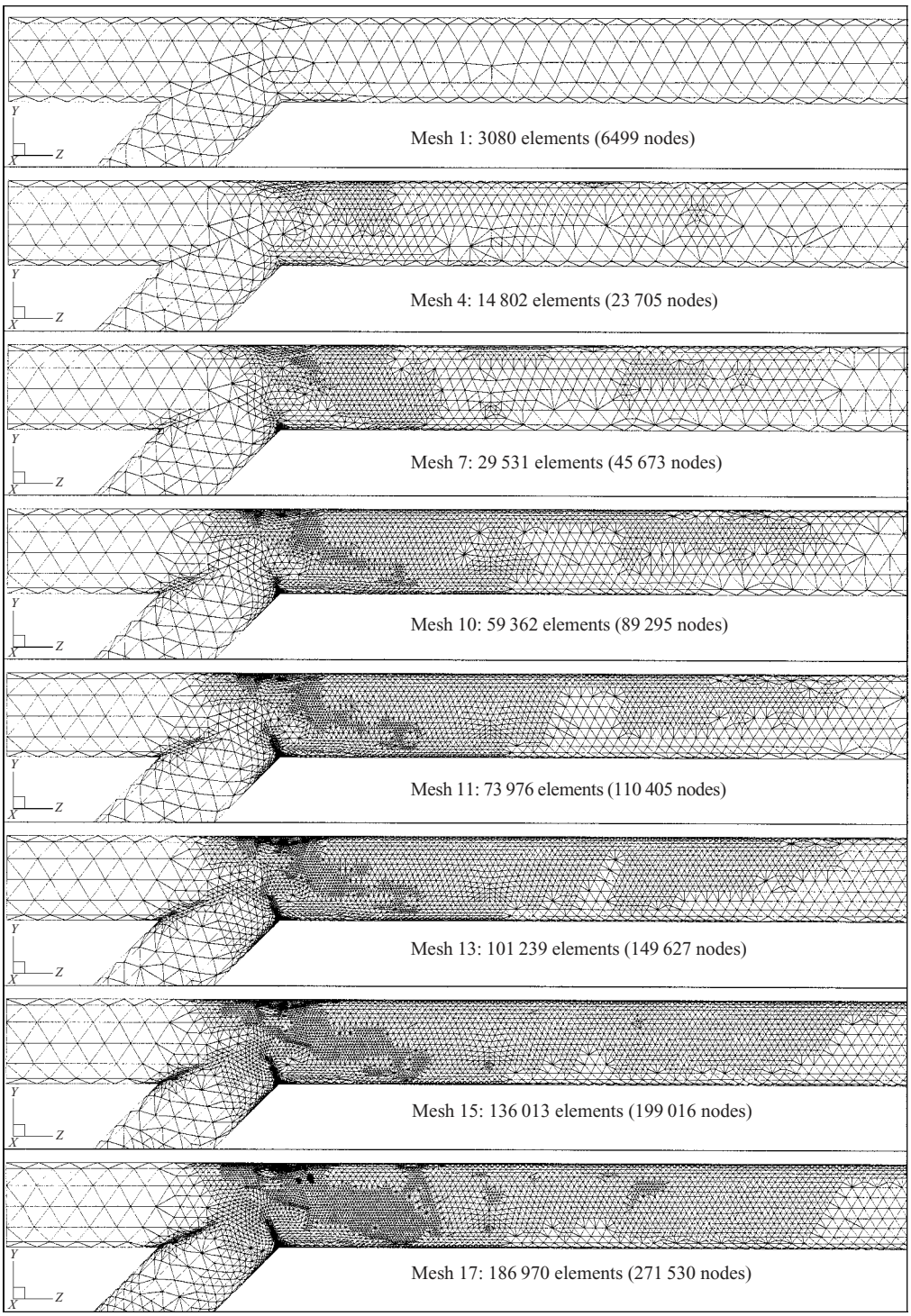

FIGURE 7. Sequence of adaptively refined finite element meshes used in the present study. The sidewalls of the graft and host tubes are visible in this view.

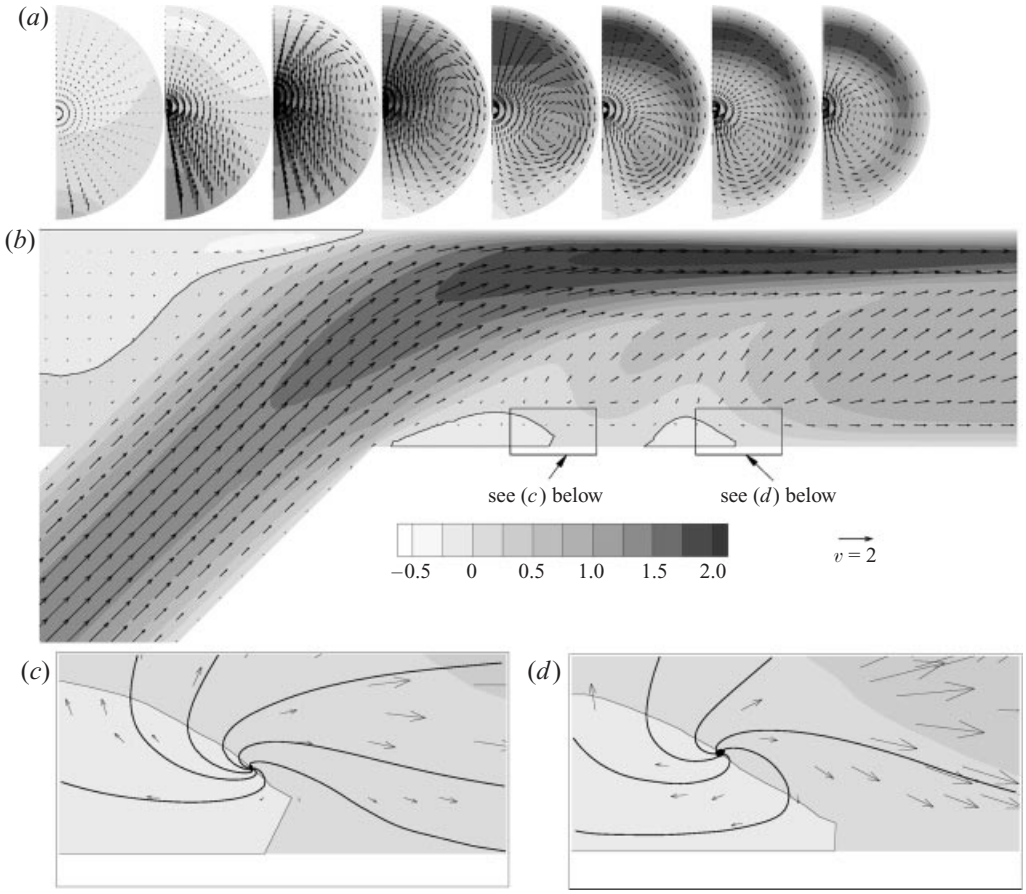

FIGURE 8. Numerically computed velocity field in the junction geometry at $Re_D = 550$. (*b*) Model symmetry plane, showing net velocity vectors overlaid with contours of axial velocity. Contours of zero axial velocity are highlighted, demonstrating two zones of retrograde flow in the host tube. (*a*) Cross-sectional slices through the host tube, showing secondary flow velocity vectors and axial velocity contours. The axial station at which each slice was extracted can be determined by extending a vertical line from the centre of each subpanel down to (*b*). Note the strong helical flows shown in the transverse sections. (*c*, *d*) Zoomed view of the distal region of the retrograde flow zones, corresponding to the boxes in (*b*). Net velocity vectors are overlaid with contours of axial velocity, upon which are superimposed streamlines in the symmetry plane. The existence of two free stagnation points is clearly seen. All velocities have been made dimensionless with respect to the mean inlet velocity. All vectors are to the same scale, except in (*c*, *d*), where the scale has been multiplied by 3.

secondary velocity magnitude at the sidewall is approximately 70% of the mean inlet velocity.†

4. For *Re* less than 250, no retrograde flow (i.e. flow from right to left in figure 8) exists downstream of the toe on the symmetry plane of the host tube.

5. For *Re* in the range 250 to 400, a single region of retrograde flow exists im-

† In the immediate neighbourhood of the junction, the definition of secondary flow is ambiguous, since it could be argued that there is no 'primary' flow direction, or even that the primary flow direction is directed along the graft tube axis. Nonetheless, to avoid complicating the notation, we refer to any fluid motions in the host tube that are transverse to the tube axis as 'secondary'. Of course, this definition is unambiguous downstream of the toe.

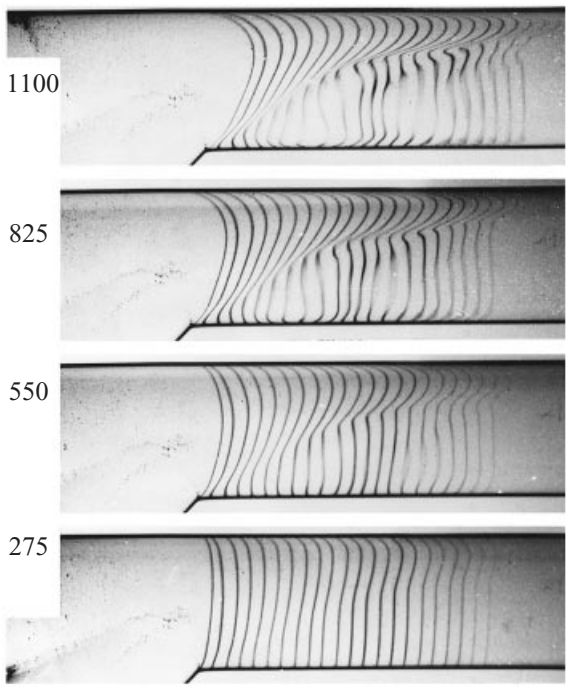

FIGURE 9. Photographs of the flow patterns in the model symmetry plane at selected Reynolds numbers (shown on the left). The flash delay used for these and subsequent photographs was 10 ms.

mediately distal to the toe of the junction. The size of this zone and the velocities within it increase with *Re*.

6. For $Re \geqslant 450$, two distinct zones of retrograde flow exist: a first zone immediately distal to the toe, and a second zone further downstream (figure 8). Although the length of the first retrograde flow zone is only very weakly dependent on *Re*, the length of the second zone increases with *Re*.

A detailed comparison of numerically computed and experimentally measured axial velocity patterns shows generally good agreement (figures 11 to 14). The agreement on the symmetry plane is particularly good, with the minor exception that the numerical results predict a slightly larger second retrograde flow zone than was measured experimentally (figure 11). The axial velocity patterns on the symmetry plane show a double-peaked profile that is reminiscent of entry flow in a curved tube (figure 12), confirming the very strong nature of the secondary flows in this geometry. Comparison of velocity profiles for the two largest finite element meshes (157 420 vs. 186 970 elements) shows that effective mesh independence was achieved for velocity field calculations (figure 12). Off the symmetry plane of the model, the experimental data show evidence of flow asymmetry (compare figures 13(*a*) and 13(*c*), and see also experimental data in figure 14). This asymmetry may explain the somewhat poorer agreement between numerical and experimental data seen at these locations. The axial velocities extracted from the plane $y/R = -0.1$ are particularly interesting (figure 14). The presence of high-momentum fluid along the sidewalls for $Z > 1$ is clearly seen, as are two 'islands' of low-momentum fluid emanating from the 'tops' of the retrograde flow zones on the symmetry plane (compare figure 11 and figure 14 at $Z = 0.9$ and 1.6).

The location of the downstream edge of the retrograde flow zone(s) in the symmetry plane shows a rather interesting dependence on Reynolds number (figure 15).

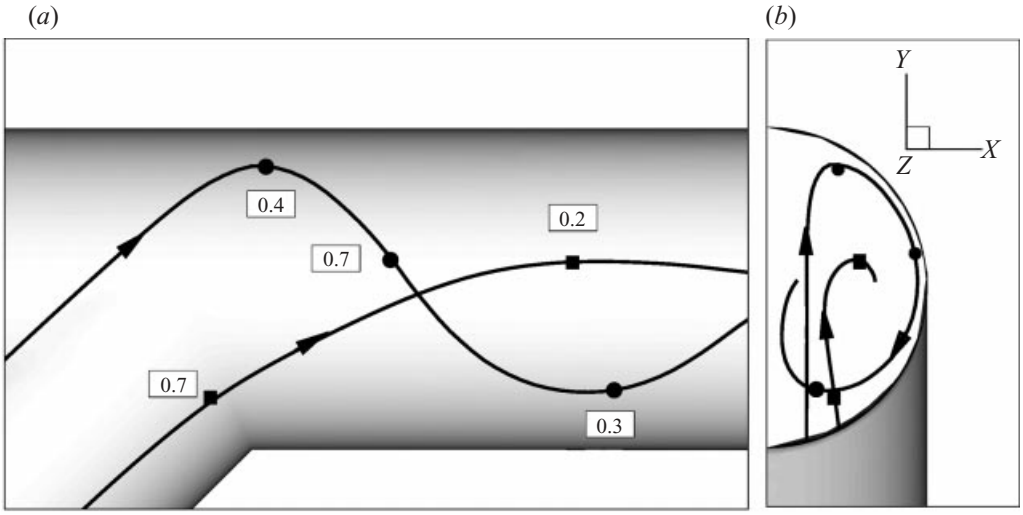

FIGURE 10. Selected streamlines in the junction geometry at $Re_D = 550$, seen from the side (*a*) and from the outflow end of the host tube (*b*). Note the helical pattern of the streamlines, causing some fluid particles to be transported to the near vicinity of the model symmetry plane. The numbers in the boxes are the magnitude of the secondary velocity relative to the mean axial velocity at the location shown by the symbol, demonstrating deceleration of the rapidly moving fluid near the sidewall as it approaches the symmetry plane.

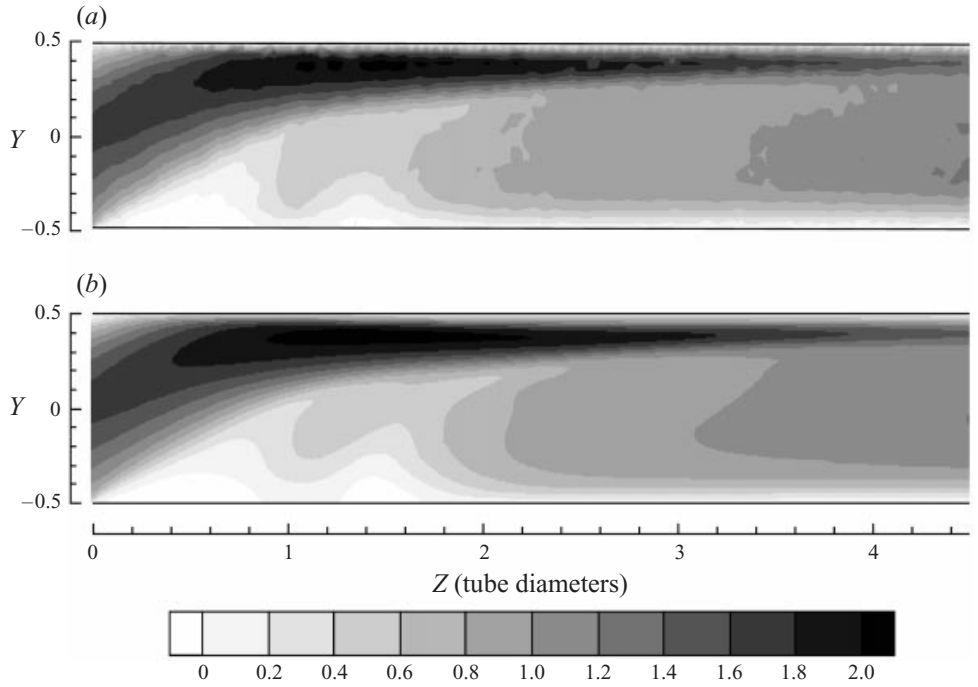

FIGURE 11. Contour plots of (*a*) experimentally measured and (*b*) numerically computed normalized axial velocities on the model symmetry plane at $Re_D = 550$. All velocities are normalized by the mean inlet velocity, and all positions are normalized by host tube diameter. Only the host tube is shown (toe at $Z = 0$).

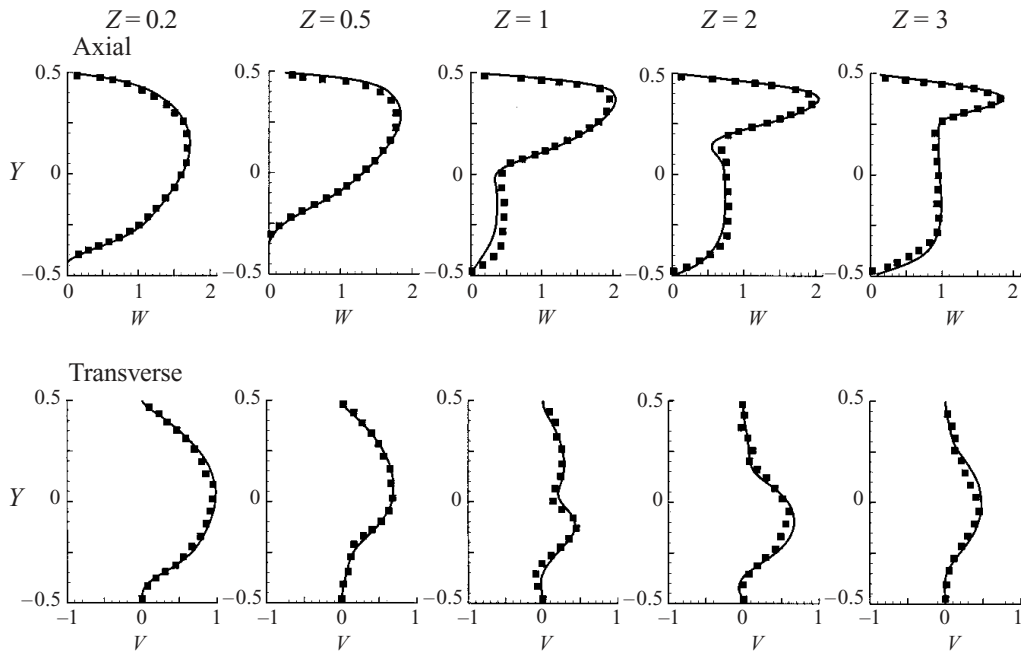

FIGURE 12. Comparison of numerically computed (solid lines) and experimentally measured (symbols) velocity profiles on the symmetry plane of the model at $Re_D = 550$. Data from two different numerical simulations on adaptively refined meshes of 157 420 (thin line) and 186 970 (thick line) elements are shown; however, only a single line is visible at almost all locations since the two lines essentially coincide. All velocities are normalized by the mean inlet velocity, and all positions are normalized by host tube diameter.

Specifically, as Re increases, the length of the first zone stops growing at the same time as the second retrograde flow zone appears; as Re further increases, the length of the first zone actually decreases slightly. This figure also allows a general comparison between numerical and experimental results. Generally, the agreement is excellent, except for the location of the first retrograde flow zone for low Re (which is somewhat underpredicted by the numerical simulations), and for the locations of the second retrograde flow zones for $Re = 450$ and 500 (which are substantially underpredicted by the numerical simulations). The reason for such a large discrepancy in the latter case is not clear, since the location of the second retrograde flow zone is well predicted at all higher values of Re.

A plot of wall shear stresses along the lower wall of the host tube on the symmetry plane vs. Re shows reasonable agreement between numerically predicted and experimentally measured values (figure 16). However, there is a consistent trend towards numerical simulations predicting smaller magnitudes for wall shear stress extrema in the range $0.6 \leqslant Z \leqslant 1.4$ than were experimentally measured. This discrepancy in wall shear stresses was puzzling, especially in light of the very favourable agreement in velocities on the model symmetry plane. We therefore considered a number of factors that could potentially explain these results, including numerical inaccuracies, experimental error in positioning the laser trace precisely on the symmetry plane of the model, and experimental error in measuring fluid viscosity (which will affect Re). We consider each of these in turn.

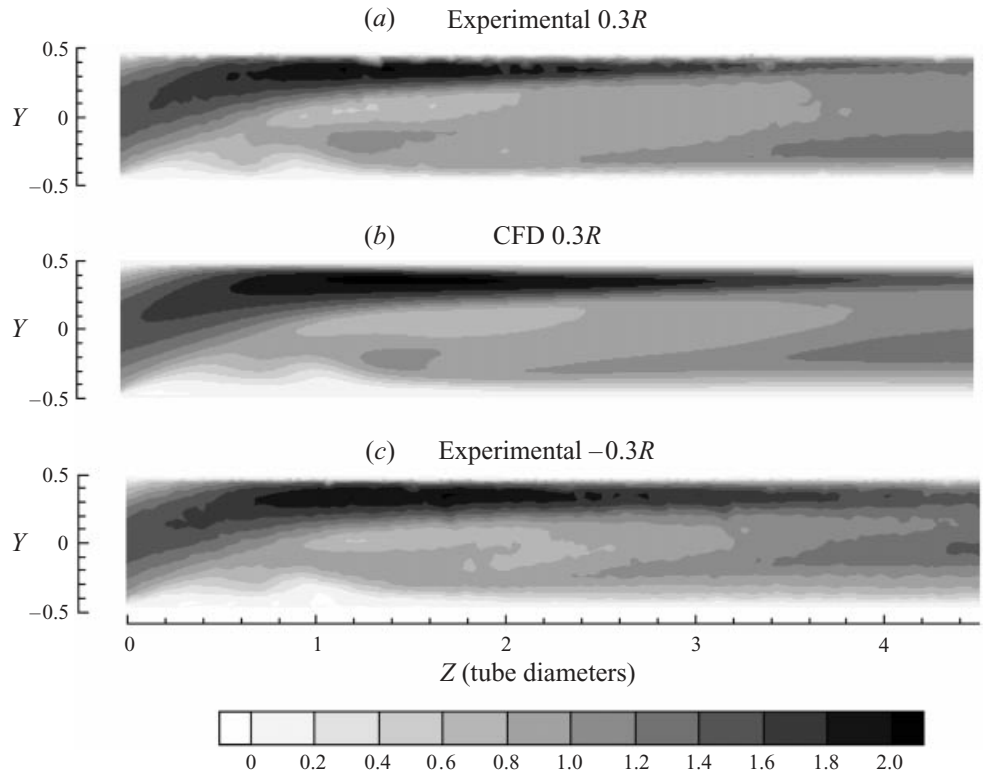

FIGURE 13. Contour plots of (a, c) experimentally measured and (b) numerically computed normalized axial velocities on planes parallel to the symmetry plane for $Re_D = 550$, at $X = \pm 0.3$ host-tube radii, R. All velocities are normalized by the mean inlet velocity, and all positions are normalized by host-tube diameter. Only the host tube is shown (toe at $Z = 0$).

Numerical inaccuracies: Preliminary studies using non-adapted meshes of successively higher densities revealed that the most significant potential source of numerical error was a spatially under-resolved finite element mesh. However, a detailed comparison of wall shear stresses on an adaptive mesh series for $Re = 550$ shows minimal mesh dependence for the higher mesh densities used in this work (figure 17*a*). We conclude that the observed experimental–numerical shear stress discrepancies are not due to under-resolved meshes.

Laser trace positioning errors: It is difficult to ensure that the laser traces are positioned precisely on the symmetry plane of the model. Further, positioning error is aggravated by the refractive index difference between the model and the working fluid, although for traces near the symmetry plane this effect is very small and can be neglected. It was estimated that the traces could have been as far as 0.1 radii away from the symmetry plane. To investigate the sensitivity of wall shear stresses to trace positioning, numerically computed wall shear stress data were extracted from the host-tube lower wall at 0.1 radii away from the symmetry plane. Some deviation from the values on the symmetry plane was noted, but the differences were generally small (figure 17*a*). We conclude that trace positioning errors cannot explain the observed wall shear stress discrepancies.

Fluid viscosity measurement errors: Errors in viscosity measurement were estimated to be approximately 10%, and we therefore carried out numerical simulations at

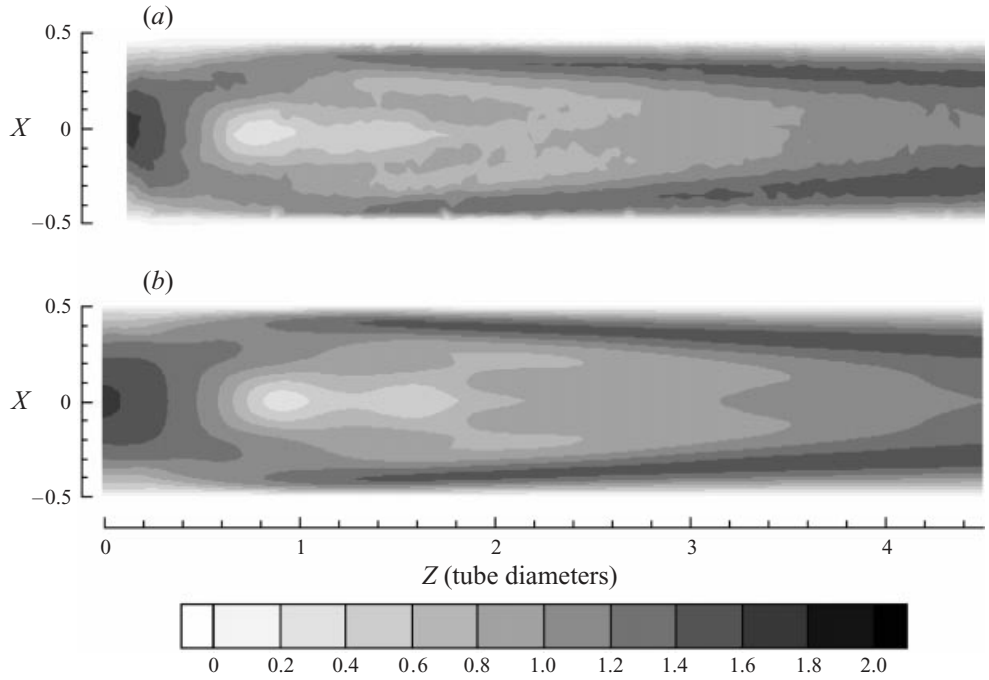

FIGURE 14. Contour plots of (*a*) experimentally measured and (*b*) numerically computed normalized axial velocities on the host-tube 'midplane' for $Re_D = 550$. This midplane is defined as the plane $y = 0$; however, due to trace positioning inaccuracy, it was determined that experimental measurements were actually made at $y/R = -0.1$, and the comparison is therefore made for this plane. All velocities are normalized by the mean inlet velocity, and all positions are normalized by host-tube diameter. The toe is located at $Z = 0$. No experimental data were gathered from the region $0 \leqslant Z \leqslant 0.1$, and it is therefore blanked out.

$Re = 500$ and 600 to bracket our $Re = 550$ results. Symmetry-plane wall shear stresses did show a slight Re dependence, but not significant enough to account for the discrepancies discussed above (figure 17*b*). We conclude that viscosity measurement errors cannot explain the observed wall shear stress discrepancies.

We will return to the issue of numerical–experimental comparison in § 4.2.

3.2. *Singular points in the velocity field*

One way of characterizing junctional flow patterns is to examine the distribution of singular points in the centreplane velocity field. These are shown for $Re = 400$, 550 and 700 in figure 18. It is known (Hunt *et al.* 1978; Tobak & Peake 1982) that the number and type of singular points in the velocity field on a plane, or in the wall shear stress field on a surface, must satisfy a constraint arising from the kinematics of the flow. In the present case this constraint takes the form

$$\sum_{nodes} + \sum_{foci} - \sum_{saddles} + \frac{1}{2}\left[\sum_{half\text{-}nodes} - \sum_{half\text{-}saddles}\right] = 0, \tag{13}$$

where $\sum_{nodes}$ represents the total number of nodal points on the surface of interest, etc. (Hunt *et al.* 1978). In this context, half-saddles and half-nodes in the symmetry-plane occur when singular points in the symmetry-plane streamline field are situated

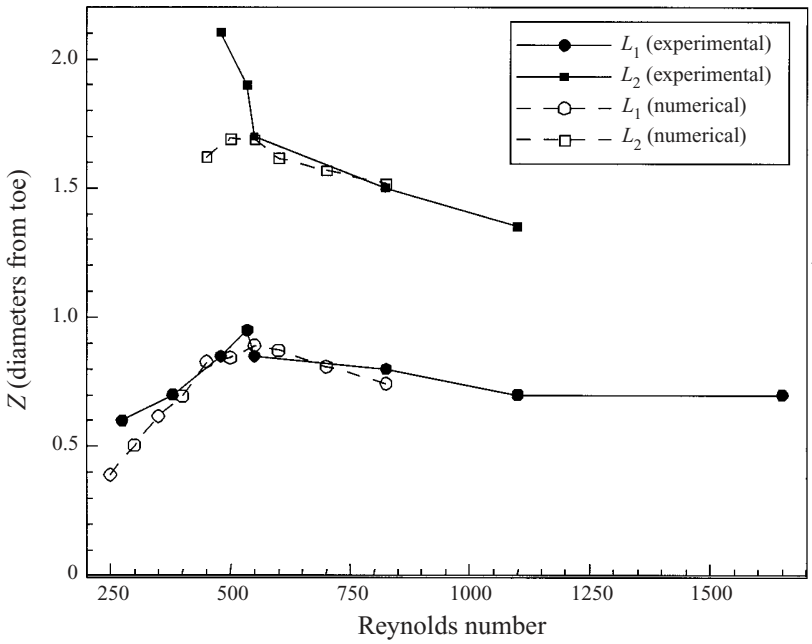

FIGURE 15. Comparison of experimentally determined and numerically computed locations of the distal (downstream) edge of the retrograde flow zone(s) as a function of Reynolds number. Locations are measured from the toe and made dimensionless with respect to tube diameter. L_1 is the location of the distal boundary of first retrograde flow zone and L_2 the location of the second, where the boundary of the retrograde flow zone is the zero-axial-velocity contour.

on solid surfaces (see figure 1). All singular point distributions in figure 18 (and in figures 20–22) satisfy equation (13).

At $Re_D = 400$, the proximal portion of the host tube demonstrates an interesting combination of foci and half-saddles, associated with the presence of vortices centred around the two foci. The leftmost vortex is extremely weak. From the streamline pattern in this region we deduce that fluid that travels retrograde from the stagnation point along the bed approaches one of the two foci. This fluid then moves in a three-dimensional fashion away from the symmetry plane, and is convected distally in the host tube. The bed stagnation point is present as a half-saddle opposite the opening of the graft tube. The most interesting singular points in the flow are those located downstream of the toe on the lower wall of the host tube, since an understanding of the flow in the neighbourhood of these points is the key to understanding axial flow separation. Just distal to the toe, there is a half-saddle (corresponding to a saddle point in the limiting streamline field on the lower wall). This marks the upstream boundary of the retrograde flow zone. Further distal to this point, there is a half-node caused by secondary boundary layer collision, as discussed in detail in § 4.1.2.

At $Re_D = 550$ (figure 18*b*), the topology of the critical points in the proximal part of the host tube is identical to that for $Re_D = 400$, although the exact location of the critical points shows a weak dependence on Reynolds number. Downstream of the toe, the half-saddle immediately distal to the toe remains. However, the half-node distal to the toe present at $Re_D = 400$ has moved away from the wall to form a full node and a half-saddle. As will be discussed below, the motion of this node away from the wall is due to secondary flow separation. This node is a free stagnation point,

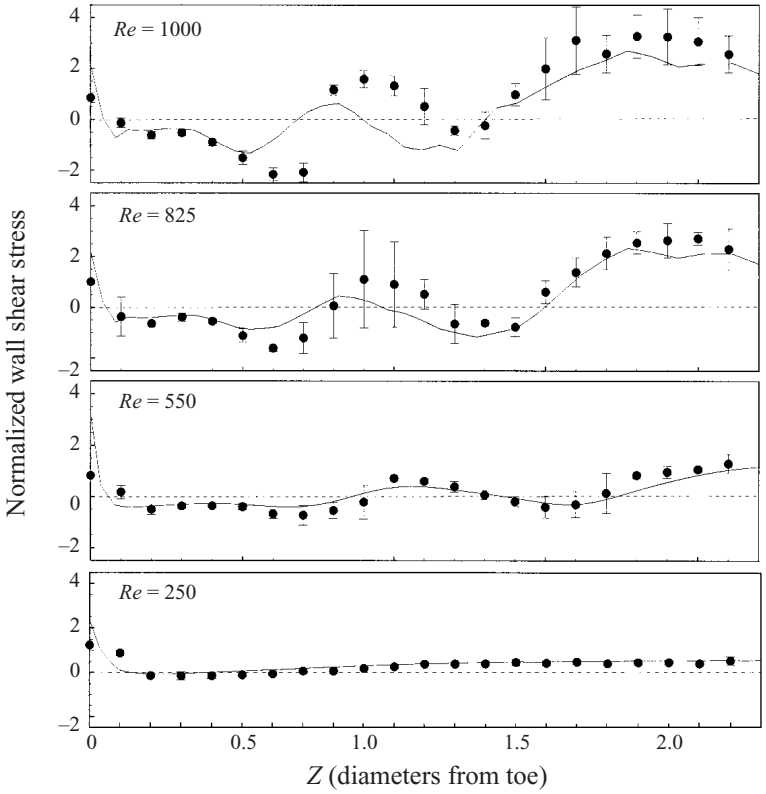

FIGURE 16. Comparison of experimentally determined (symbols) and numerically computed (lines) normalized wall shear stresses on the model symmetry plane along the lower wall for selected *Re*. Symbols denote the mean of five experimental measurements, and error bars represent 95% confidence limits. The normalized wall shear stress is defined to be the wall shear stress divided by the shear stress that would exist in Poiseuille flow in a tube of diameter D at the same *Re*.

i.e. a stagnation point removed from a solid surface, associated with the delivery of fluid towards the symmetry plane from both halves of the geometry by strong helical secondary flows. Also noteworthy is the formation of a second triplet of critical points (two half-saddles and a node) further distal from the toe. These critical points are associated with the second retrograde flow zone. It can be seen that the topology of critical points in the second retrograde flow zone is identical to that of the first zone.

At $Re_D = 700$, the topology of all critical points is identical to that at $Re_D = 550$, although the locations are slightly different than at $Re_D = 550$. It is interesting to note that the singular points in the proximal portion of the host tube (including the half-saddle associated with the bed stagnation point) by themselves satisfy equation (1), as do the singular points downstream of the toe. This reinforces the idea that the slow-moving fluid in the proximal portion of the host tube communicates only weakly with the main flow.

3.3. *Wall shear stress patterns*

Insight into the physics of flow separation is aided by studying wall shear stress and limiting streamline patterns within the junction, as obtained from numerical simulations. In figure 19 we plot contours on which the axial component of the wall shear stress is zero as a function of *Re*. Immediately adjacent to the wall, fluid within

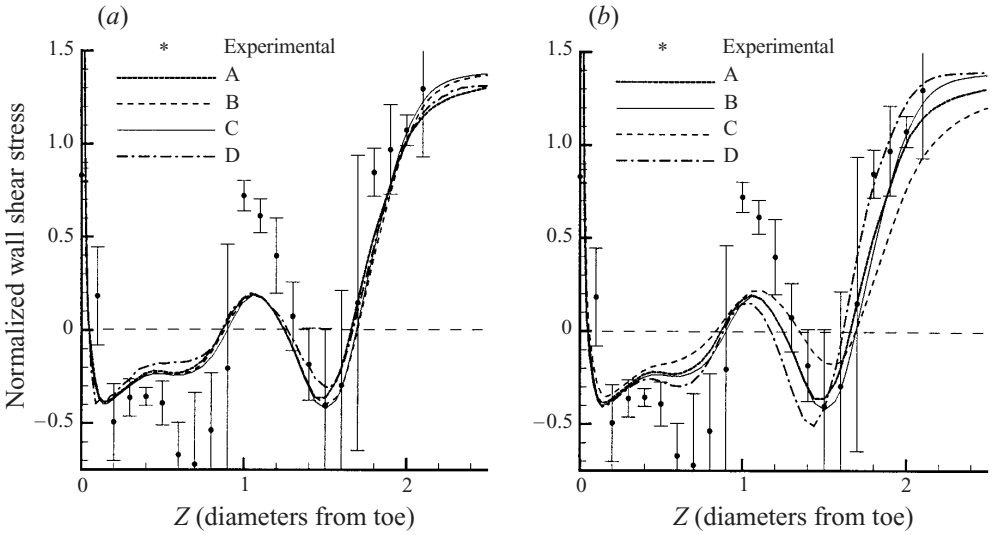

FIGURE 17. Comparison of experimentally determined and numerically computed normalized wall shear stresses on the model symmetry plane along the lower wall at $Re_D = 550$. (*a*) The effects of mesh refinement (lines A–C) and extraction location (line D) on normalized wall shear stress. A: 117916 element adapted mesh; B: 157420 element adapted mesh; C: 186970 element adapted mesh; D: 186970 element adapted mesh (shear stress extracted at a distance of $0.1R$ from the symmetry plane). (*b*) The effects of small variations in Reynolds number on normalized wall shear stress. A: 117916 element adapted mesh ($Re = 550$); B: 186970 element adapted mesh ($Re = 550$); C: 117916 element adapted mesh ($Re = 500$); D: 117916 element adapted mesh ($Re = 600$). See figure 16 for explanation of symbols and error bars.

these contours flows in the retrograde direction, and thus these contours can be considered as the 'footprint' of the retrograde flow zones. The number and extent of these retrograde zones are consistent with the above qualitative descriptions of flow on the symmetry plane (e.g. figure 15). There are several noteworthy points about this figure. The location of the proximal boundary of the first retrograde flow zone is essentially independent of *Re*, while the location of the distal boundary depends on *Re* (cf. figure 16). The distal boundary of the second retrograde flow zone is only weakly dependent on *Re*, and thus the second zone enlarges with *Re* primarily by growth in the proximal direction. For $Re \geqslant 700$, the second retrograde flow zone appears to be interacting strongly with the first zone, and enlarges by developing 'legs' that extend proximally and circumferentially.

It is useful to characterize singular points of wall shear stress in this flow as a function of Reynolds number. We begin by examining the situation at $Re_D = 400$, for which there is only one retrograde flow zone distal to the toe. There is a total of eight singular points, as shown in figure 20. The heel is a saddle point (S_1), as is the point where the two counter-rotating vortices in the proximal host tube meet on the upper wall of the symmetry plane (S_3). The stagnation point on the bed of the host tube is a nodal point (N_4), as is an attachment point on the lower wall of the proximal portion of the host (N_2 – just out of field of view in figure 20*b*). The retrograde flow zone is associated with two saddle points (S_5 and S_7), as well as two foci (F_6 and its mirror image). All saddle points except for S_7 are separation points in the terminology of Hunt *et al.* (1978), while all the nodal points and foci are attachment points. The limiting streamlines of separation and attachment divide the surface of

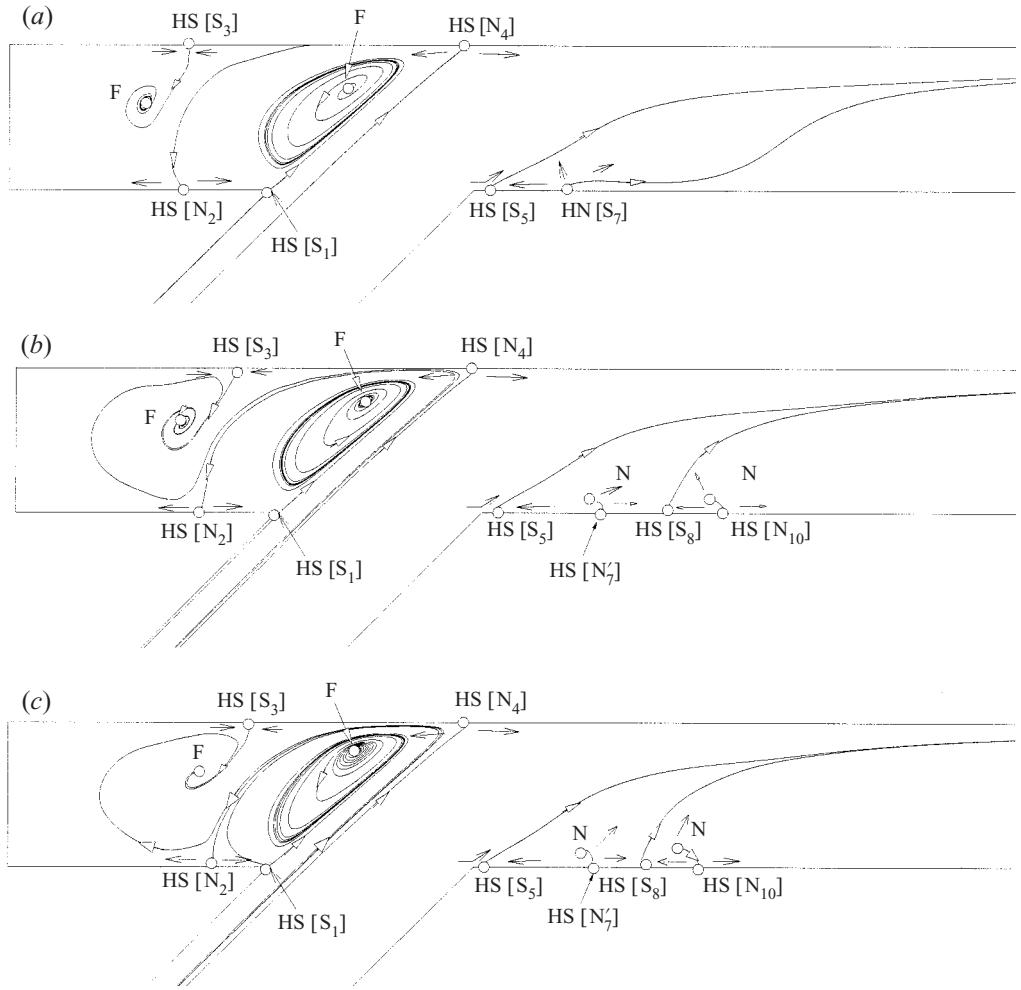

FIGURE 18. Distribution of critical points on the symmetry plane of the model at (*a*) $Re_D = 400$, (*b*) 550 and (*c*) 700, plotted to scale based on numerical data. F, S, HS, N, and HN refer to focal, saddle, half-saddle, nodal, and half-nodal points respectively. Lines are streamlines in symmetry plane; arrows are qualitative descriptors indicating the direction (but not magnitude) of the symmetry-plane velocity field. The bracketed terms following the half-saddles and half-nodes are cross-references to the corresponding critical points in the surface wall shear stress field (see figures 20–22).

the geometry into eight distinct regions (four on each side of the symmetry plane), which communicate only through fluid exchange from the bulk. The distribution of critical points on the surface is complex, and understanding of these points can be facilitated by comparison with the critical points in the symmetry-plane streamline field (figure 18*a*). For example, saddle points S_5 and S_7 correspond to the half-saddle and half-node immediately downstream of the toe shown in figure 18(*a*). To facilitate this comparison, all singular points on solid surfaces in figure 18 are labelled with their corresponding points in figures 20–22.

As the Reynolds number increases, a second retrograde flow zone forms (figure 21). This second zone has associated with it a saddle and a node on the symmetry plane (S_8 and N_{10}), as well as two symmetrically placed foci (F_9 and its mirror image)

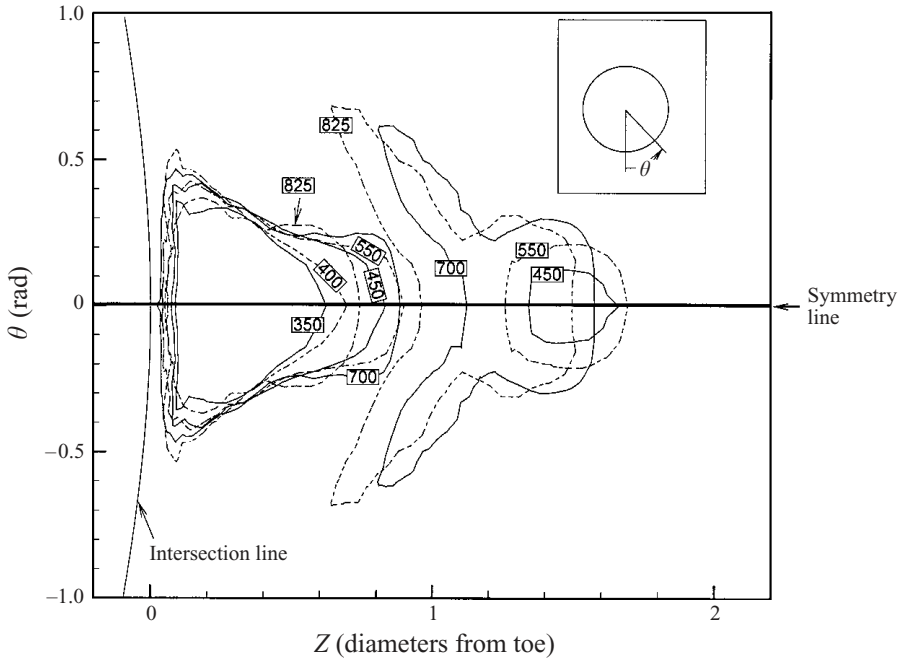

FIGURE 19. Contours of zero axial shear stress on the lower wall of the host tube for the indicated Reynolds number, *Re*. θ is defined to be the angular position of a point on the wall, measured with respect to the symmetry plane of the model, as shown in the inset. The 'intersection line' is the curve where the graft tube and the host tube meet, while the 'symmetry line' is the intersection of the symmetry plane and the lower wall of the host tube. The toe of the junction is the point where the intersection line crosses the symmetry line, at $\theta = Z = 0$. Note the upstream extension of the 'legs' extending from the second retrograde flow zone for $Re \geqslant 700$.

and two symmetrically placed saddles (S_{11} and its mirror image). Coincident with the formation of this second zone, saddle point S_7 splits to form a node on the symmetry plane (N_7') and two symmetrically placed saddles (S_7' and its mirror image). Here we denote by a prime a critical point obtained by bifurcation of an existing point at a lower *Re*. Thus, N_7' and the two S_7' originated from the bifurcation of S_7 at $Re_D = 400$. At $Re = 450$ (not shown), which is only slightly larger than the critical *Re* at which the second zone forms, N_7' and the two S_7' lie almost atop one another, and then move apart as *Re* increases to 550. The total number of critical points is now 16 (eight saddles, four foci, four nodal points). The limiting streamlines of separation and attachment divide the surface into 18 zones (nine on each side of the symmetry plane).

As the Reynolds number increases beyond 700, the shape of the second retrograde flow zone changes, with the formation of 'legs' that extend circumferentially and proximally (figure 22). The total number of critical points and streamlines of separation and attachment is the same as for the $Re_D = 550$ case. From examination of the solid and dashed contours in figures 20–22 it can be seen that there is separation of both the axial (primary) and secondary flows.

3.4. *Vorticity distribution*

Vorticity transport in this flow is somewhat complex. We illustrate some of the main effects by showing contours of θ, Z and radial (r) components of vorticity at selected

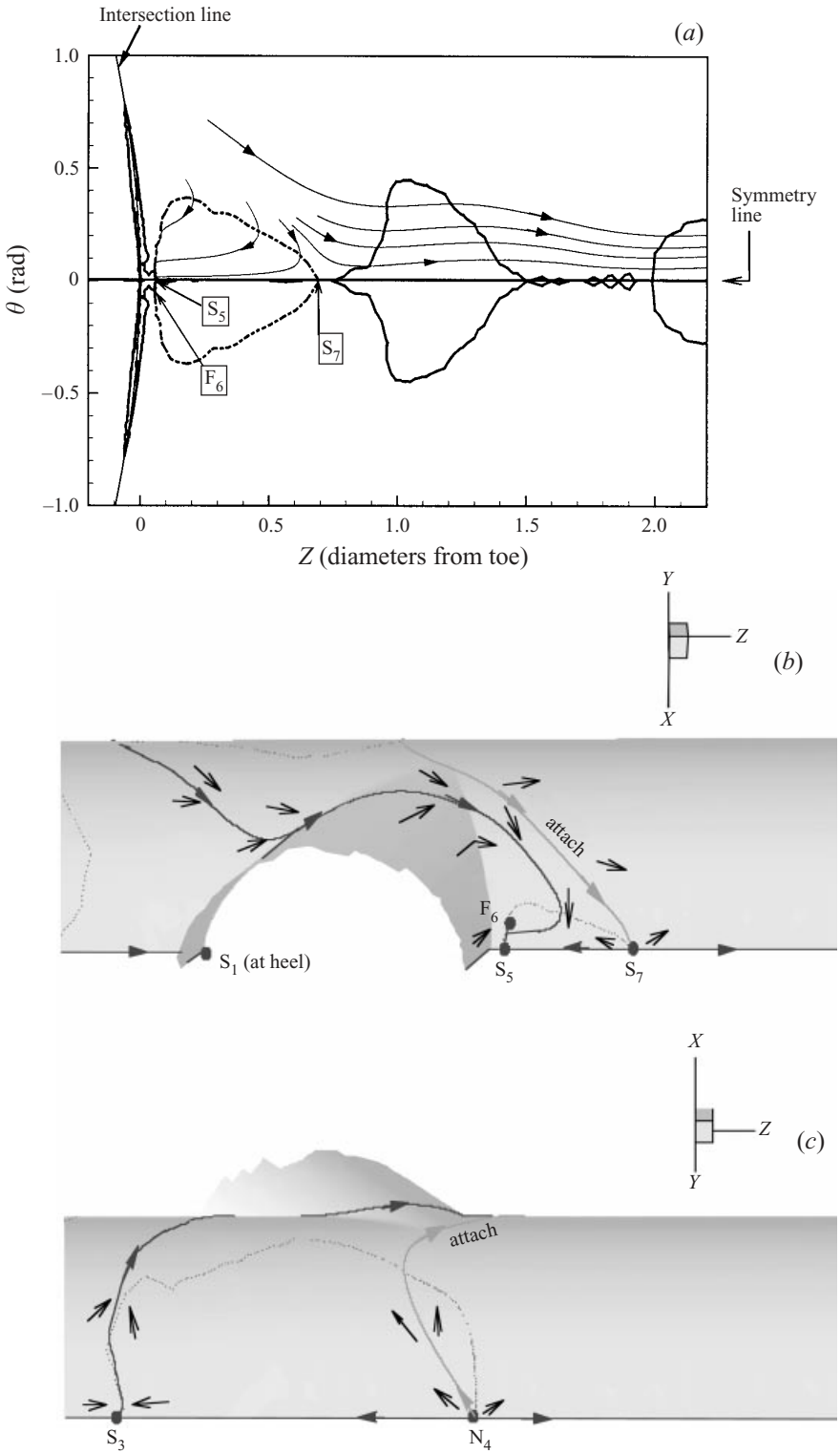

FIGURE 20. For caption see facing page.

cross-sections in the host tube in figure 23 for $Re_D = 700$. At the toe ($Z = 0$), the θ-component, associated mainly with axial flow velocity gradients, is very similar to that expected for Poiseuille flow, with two minor exceptions. First, there is a slight displacement of the zero vorticity contour away from the tube centre towards the upper wall. Second, there is a small region of fluid at the lower wall that has very substantial θ-vorticity, generated by flow over the sharp toe. At $Z = 0.2$, this zone of large θ-vorticity has been displaced away from the lower wall by the first retrograde flow zone, while the vorticity magnitude in this fluid region has been attenuated by viscous effects (see lower contour 3 at $Z = 0.2$ in figure 23*a*). Meanwhile, a zone of zero θ-vorticity associated with the retrograde flow zone has developed on the lower wall, leading to a 'two-layer' vorticity structure along the lower wall. Further downstream ($Z > 0.2$), the cross-sectional shape of the axial flow separation region, particularly the 'legs' of the second retrograde flow zone, are reflected in the zero contours of vorticity near the lower wall (compare figures 22 and 23*a*). However, the dominant θ-vorticity feature for $Z \geqslant 0.2$ is the generation of large θ-vorticity values in a boundary-layer-like region† along the upper and side walls. As this fluid travels downstream its vorticity diffuses away from the wall, as well as being convected along the sidewalls by secondary flow. At $Z \approx 0.7$ the secondary flow separates from the sidewall, and high-θ-vorticity fluid is carried away from the wall. Due to nonlinear effects, some of this θ-vorticity is converted to r-vorticity, leading to a concentrated zone of large r-vorticity at $Z = 0.8$ (see contour 5 at $Z = 0.8$ in figure 23*c*).

The distribution of Z-vorticity is somewhat different (figure 23*b*). Z-vorticity is associated almost exclusively with the secondary flow boundary layer on the sidewall, which can be seen to spiral down the host tube. One interesting feature of the Z-vorticity distribution is the presence of a zone of fluid with negative Z-vorticity near the sidewall at $Z = 0$ and 0.2. This is due to fluid with negative Z-vorticity being entrained from the proximal portion of the host tube. The decay of Z-vorticity with distance down the host tube is more rapid than the decay of θ-vorticity.

Finally, in figure 23(*c*), we show the r-component of vorticity. Immediately downstream of the toe ($Z < 0.8$), there is essentially no r-vorticity. As discussed above, at $Z = 0.8$ substantial r-vorticity is generated by nonlinear effects as fluid elements with appreciable Z- and θ-vorticity separate. In fact, the generation of r-vorticity is extremely intense near the proximal focal point seen in the second retrograde flow zone (figure 22). This high-r-vorticity fluid is convected along the edge of the second

† We refer to boundary-layer like regions, rather than simply boundary layers, since there is appreciable non-zero vorticity outside of these thin regions.

FIGURE 20. Wall shear stress field, critical points and limiting streamlines in the junction geometry at $Re = 400$, plotted to scale based on numerical data. (*a*) Enlarged view of the region distal to the toe on the lower wall, using the same coordinate system as in figure 19. Contours of zero axial and circumferential components of wall shear stress are indicated by dashed and solid lines, respectively. In the upper half, selected limiting streamlines are shown; in the lower half, critical points are labelled. Compare these critical points with corresponding labels in figure 18. (*b*, *c*) Three-dimensional view of critical points in the junction: (*b*) lower wall, (*c*) bed. Solid lines overlain with arrows are limiting streamlines of separation and attachment. Arrows are qualitative descriptors indicating the direction (but not magnitude) of shear stress field. There is a limiting streamline of separation that originates at S_1 and travels along the junction of the two tubes that is only partially visualized in this view. Legend: S – saddle point; N – nodal point; F – focus point; attach – limiting streamline of attachment.

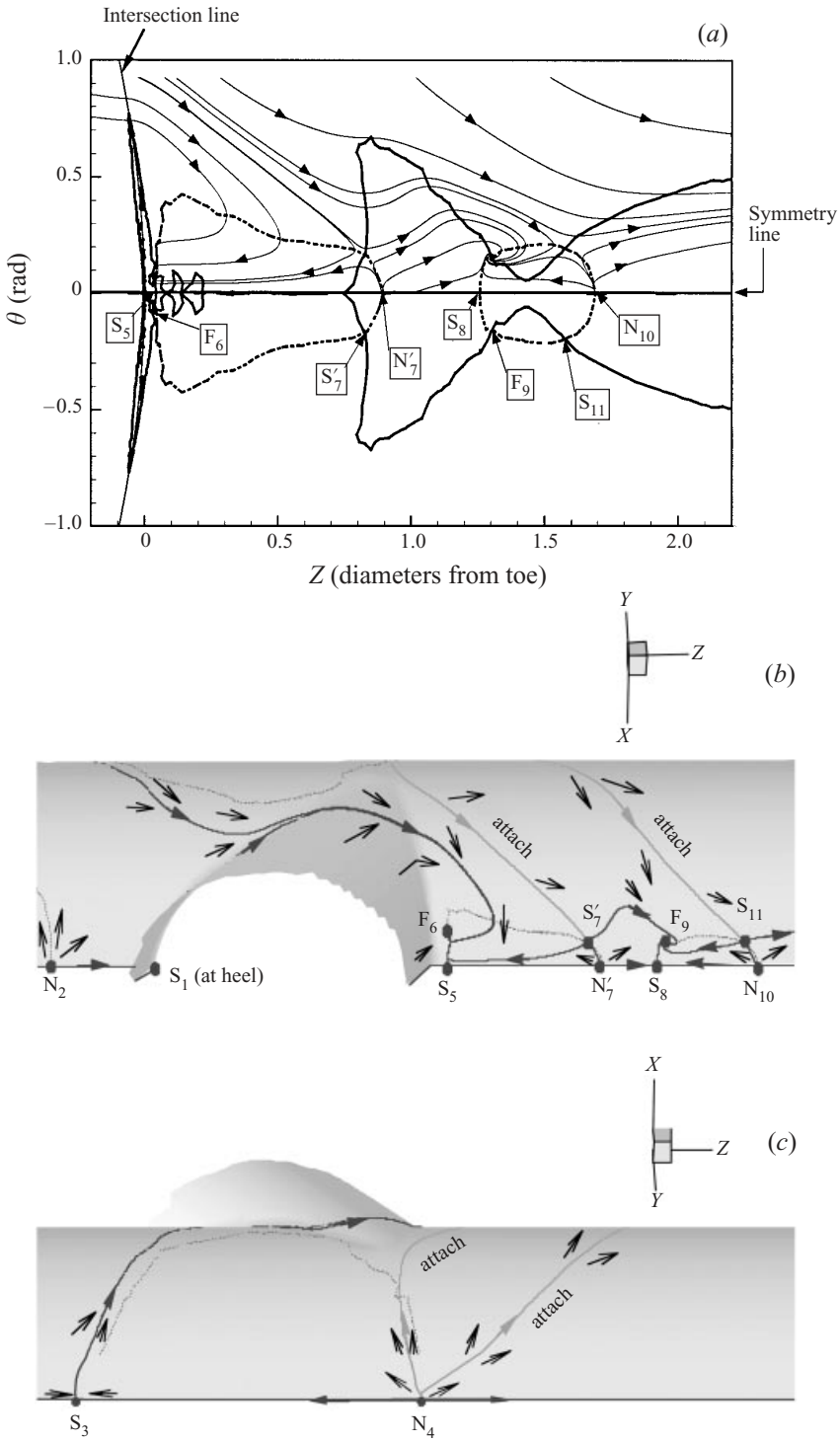

FIGURE 21. As figure 20 but at $Re = 550$.

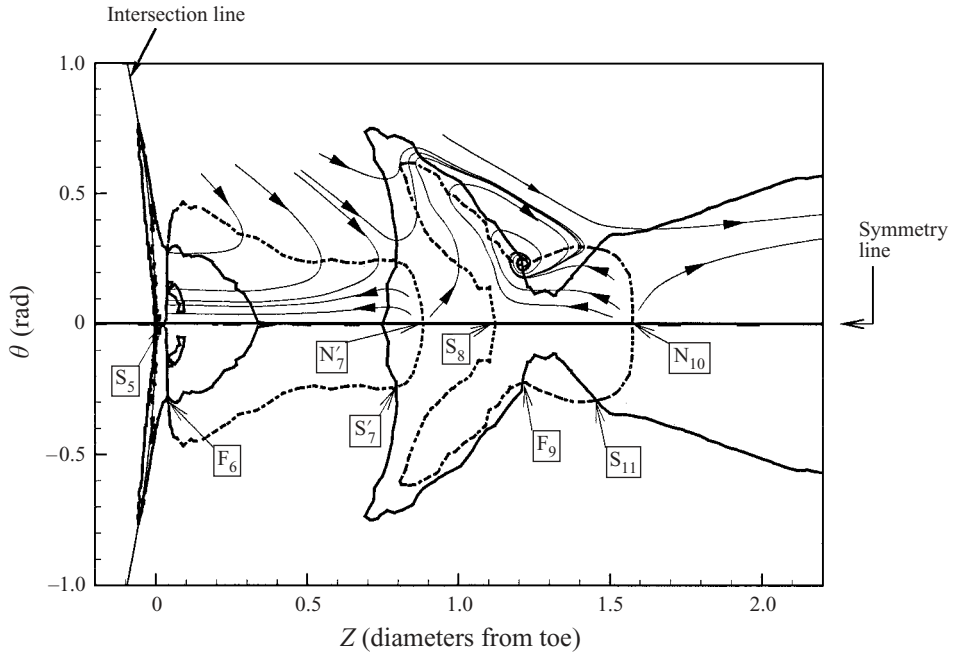

FIGURE 22. As figure 20(*a*) but at $Re = 700$. Three-dimensional view (b, c) is not shown since it is very similar to that of figure 21(b, c).

retrograde flow zone (figure 23*c*). As this occurs, the magnitude of r-vorticity grows, apparently due to viscous shearing associated with the lateral edge of the second retrograde flow zone. The presence of localized regions of large r-vorticity can be used to explain the 'smearing' of photochromic traces seen experimentally, e.g. at $Re = 550$ for the 5th to 7th traces from the right in figure 9. Although the traces were positioned within the plane of symmetry, the trace dimension into this plane was roughly two times the width (Z-dimension) of the traces. This finite width, in combination with large r-vorticity near the symmetry plane, leads to a twisting of the traces, which appears on photographs as trace 'smearing'.

In summary, vorticity in this flow is generated primarily by axial and secondary flow boundary-layer-like structures on the upper and side walls of the host tube distal to the toe. This vorticity is convected in a spiral path along the sidewalls by the high-momentum fluid that originally impacted on the bed of the host tube. Secondary flow separation at $Z \approx 0.7$ causes this fluid with large θ- and Z-vorticity to be convected away from the wall. As the fluid leaves the wall, nonlinear effects partially transform the θ- and Z-vorticity into r-vorticity, which is then convected towards the symmetry plane of the model.

3.5. *Transition to unsteadiness*

Experimentally, we searched for evidence of unsteadiness by carrying out repeated runs at selected Re, and then carefully comparing photochromic traces taken at different times and in different runs. If traces were highly repeatable from image to image at a given Re, then we concluded that unsteadiness was not present. Transition to unsteadiness was seen at $Re_D = 1650$ but not at $Re_D = 1100$, as indicated in figure 24, in which three different images for $Re_D = 1100$ and 1650 reveal a steady and an

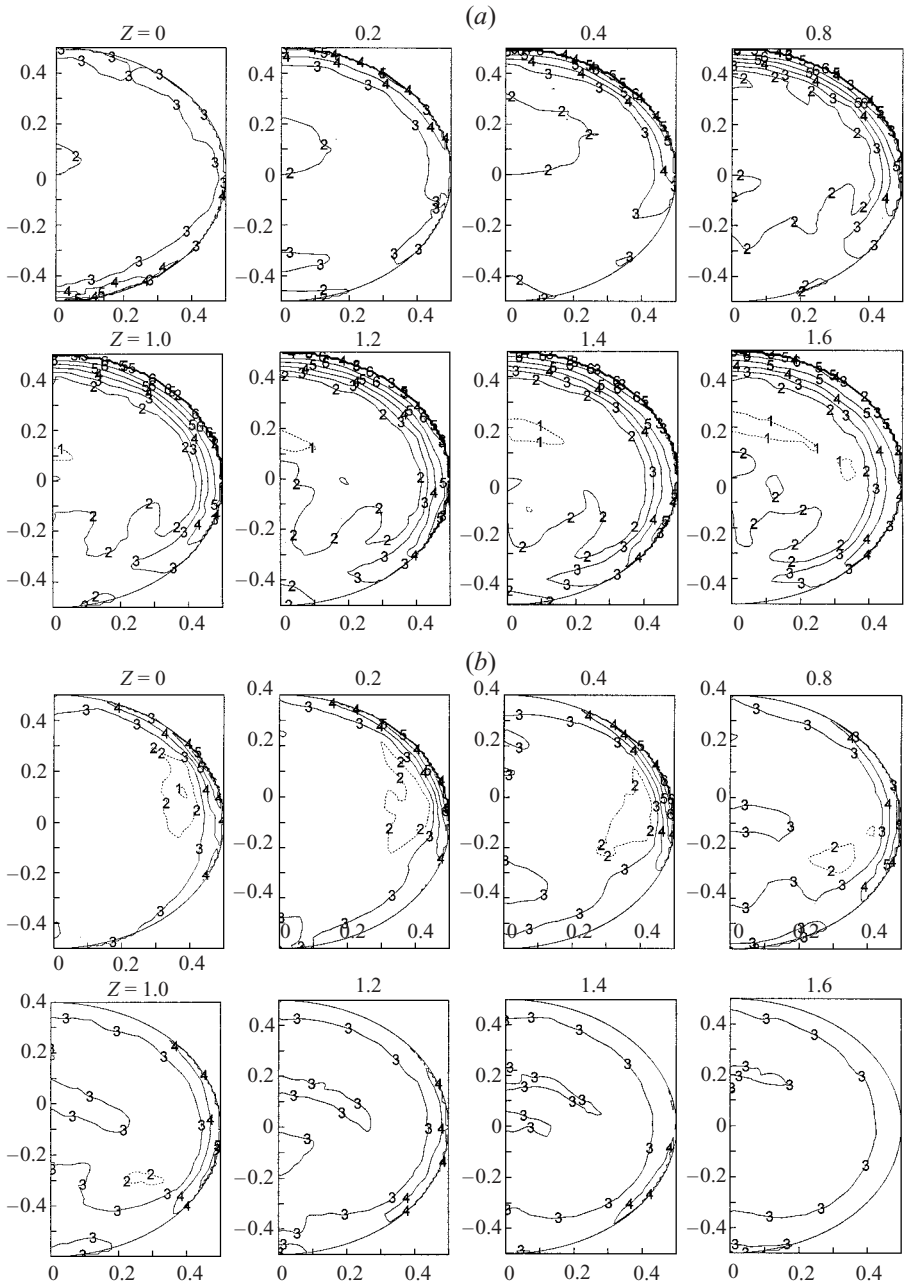

FIGURE 23. For caption see facing page.

unsteady flow field, respectively. Characteristic features during the transition stage included unsteadiness of the shear layer and the shedding of a vortex along the upper wall, similar to the observations of Pauley *et al.* (1990). The top frame in figure 24(*b*) shows the presence of a single separation vortex, while the other two frames appear to be photographed at instants of vortex shedding and as such indicate a multiple vortex structure. Figure 25 shows that further downstream (beyond $Z/D = 2$), the flow

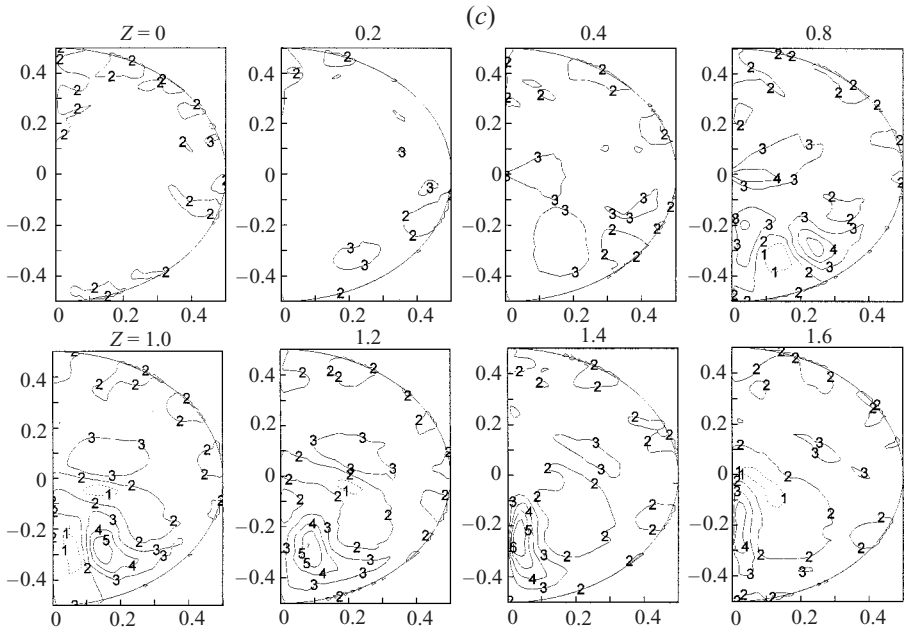

FIGURE 23. (*a*) θ- (*b*) Z- and (*c*) r-components of vorticity on selected slice planes through the host tube for $Re = 700$. The vorticity has been normalized by U/D. (*a*) Label 1, $\omega_\theta = -4$; 2, 0; 3, 4; 4, 8; 5, 12; 6, 16. (*b*) Label 1, $\omega_Z = -10$; 2, -5; 3, 0; 4, 5; 5, 10; 6, 15. (*c*) Label 1, $\omega_r = -1.6$; 2, 0; 3, 1.6; 4, 3.2; 5, 4.8; 6, 6.4.

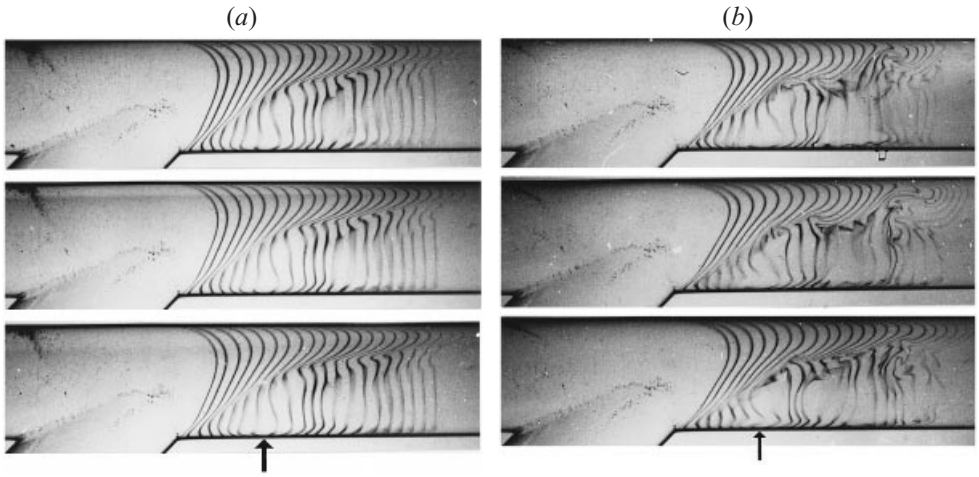

FIGURE 24. Photographs taken at three different instants for (*a*) $Re = 1100$ and (*b*) $Re = 1650$. Note the very good agreement between the images in (*a*), confirming the steady nature of the flow at $Re = 1100$. The flow is clearly unsteady at $Re = 1650$; the upper two frames of (*b*) show a rapidly moving flow structure which we hypothesize is a shed vortex (open arrow). Bold arrow indicates the distal boundary of the first retrograde flow region.

remained laminar and began to redevelop for $Re_D = 1100$, whereas, for $Re_D = 1650$, the wall jet broke down and it appeared that transition to turbulence was initiated. These observations differ from those in other studies of internal flow separation, in that our results show that the existence of multiple separation zones and the

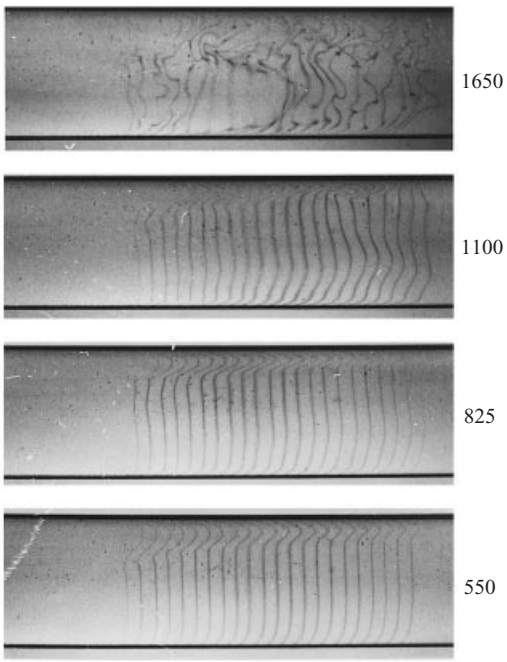

FIGURE 25. Flow patterns further downstream at selected Reynolds numbers. In these images, the leftmost trace is positioned approximately 2 diameters downstream of the toe.

'shrinkage' of the first separation zone with increasing *Re* were not associated with unsteadiness.

4. Discussion and conclusions

Flow separation in this junction geometry is highly complex and shows many features not present in a 'classical' separated flow.† Although the existence of a single separation zone distal to the toe was expected, the presence of a second separation structure at higher Reynolds numbers was somewhat surprising (Ojha 1995). Even more surprising was the fact that the formation of a second separation zone did not coincide with transition to unsteadiness, as is usually the case. These facts can be explained by the observation that separation is critically dependent on the existence of strong secondary flows, and in some sense is 'driven' by secondary flow. Several conclusions follow from this point:

Although only the case of a 45° junction has been considered in this work, we expect that any junction in which sufficiently strong secondary flows exist will show two such separation zones. The location and size of the secondary separation zone will depend both on junction geometry (angle) and Reynolds number.

The dynamics of the separation process are not dependent on the detailed geometry of the junction line between the two tubes, but instead are determined mainly by bulk flow patterns in the host tube. In particular, the existence of multiple separation zones

† By a classical separated flow we mean a flow characterized by two-dimensional separation in which there is a well-defined separation streamline that divides the flow into two non-communicating regions.

at higher Re does not depend on the 'sharpness' of the toe region. We have confirmed this latter point by simulating flow in a junction identical to that considered in the present study, with the exception that the junction line between the two tubes had rounded corners.

The size of the retrograde flow zones seen in figure 19 can be explained in terms of secondary flow effects. Generally, the relative magnitude of secondary flow velocities increases with increasing Re. At low Re ($Re_D \leqslant 400$), this causes an increase in the magnitude of the local adverse pressure gradient, and therefore growth of the first retrograde flow region. At somewhat higher Re ($450 \leqslant Re_D \leqslant 650$), a second retrograde flow region forms as secondary flows become even stronger. This second region enlarges with increasing Re, until it begins to interact with the first region, for $Re_D \geqslant 700$, at which point the first region begins to shrink. For these large Re, the second region is constrained to grow by extension of the 'legs' previously described. We speculate that transition to unsteadiness, which we have shown to develop at $Re_D \approx 1650$, may be associated with an instability initiated in these legs, although the precise mechanism for such instability is not clear.

4.1. *Comparisons with entry flow in a curved tube*

Entry flow in a curved tube or duct is a classical fluid mechanical problem that has been extensively studied by a number of authors; for reviews see Berger, Talbot & Yao (1983) and Ito (1987). The flow examined in this paper is closely analogous to entry flow with Poiseuille inlet velocity profile in a circular tube of strong curvature, especially since the flow in the proximal portion of the host tube appears to have minimal effect on separation patterns distal to the toe. It is therefore of interest to compare the axial flow separation seen in this study with the details of entry flow in curved ducts or pipes.

4.1.1. *Previous studies of entry flow*

Stewartson, Cebeci & Chang (1980) considered entry flow in a curved tube in the asymptotic limit of small curvature ratio, a/R, and high Dean number, $\kappa = Re(a/R)^{1/2}$, where a is the tube radius and R is the radius of curvature of the tube following the notational convention of Berger *et al.* 1983. Their analysis assumed an irrotational core flow surrounded by a three-dimensional boundary layer, consistent with the case of flow entering from a large reservoir into the curved section. They predicted a collision of the secondary flow boundary layers on the symmetry plane at a finite distance from the inlet, at which point the streamwise (axial) wall shear stress vanished, presumably indicating axial flow separation. The structure of this separation region was further elucidated by Stewartson & Simpson (1982), who suggested that the axial flow boundary layer was 'lifted away' from the tube wall by the secondary flow boundary layers colliding underneath it. Yao & Berger (1988) and Kluwick & Wohlfart (1984) extended Stewartson *et al.*'s calculations to the case of finite curvature ratios. For $a/R < 0.5$, Yao & Berger predicted that the location of the point of zero axial wall shear stress would move closer to the inlet; for larger values of a/R it would begin to move downstream. For finite a/R, separation was due to the collision of secondary flow boundary layers, as originally proposed by Stewartson *et al.* for the case of asymptotically small a/R (Stewartson *et al.* 1980).

All of the above studies are boundary layer analyses valid in the limit of large Dean number. Other investigators have numerically solved the full Navier–Stokes equations (e.g. Soh & Berger 1984; van de Vosse *et al.* 1989), or partially parabolized approximations thereof (e.g. Humphrey, Iacovides & Launder 1985; Liu & Masliyah

1996), for a variety of curvature ratios, Dean numbers and inlet flow conditions. Although there were some difficulties with mesh resolution (particularly at high Dean numbers (Humphrey *et al.* 1985)), axial flow separation was not predicted in any of these studies. For larger Dean numbers (in the range 600 to 2100) these studies showed a clear trend towards a point of minimum (but non-zero) axial shear stress at a finite distance from the inlet. One could therefore speculate that if the calculations were extended to higher Dean numbers, axial flow separation might have been seen. We conclude that these calculations are not inconsistent with the predictions of the boundary layer theories.

Velocity and wall shear stresses have also been studied experimentally for entry flow in curved tubes. Talbot & Wong (1982) measured wall shear stress along the inner wall of a curved pipe with $a/R = 1/7$. No axial flow separation was seen for $\kappa \leqslant 1622$. Talbot and Wong's data agreed very well with Yao & Berger's boundary layer calculations upstream of the point of zero axial wall shear stress (Yao & Berger 1988). However, agreement downstream of this point was poor. Agrawal, Talbot & Gong (1978) also observed no axial separation, although secondary separation was seen at $\kappa = 678$ and $a/R = 1/7$. Tanishita *et al.* (1991) observed secondary separation for entry flow in a curved pipe with $a/R = 1/2$; however, no axial flow separation was noted. In that study, the maximum secondary velocities were 90% of the mean inlet velocity, which again is slightly less than that seen in the present study for $Re = 550$. Other studies (Bovendeerd *et al.* 1987; Choi, Talbot & Cornet 1979; Kluwick & Wohlfart 1986; Olsen & Snyder 1985) with Dean numbers < 2900 and a variety of inlet flow boundary conditions found no evidence of axial flow separation. Eventually, of course, axial flow separation is observed at sufficiently large Dean numbers, e.g. Tananayev, Gontsov & Marinova (1982), who studied flow in a pipe bend for $\kappa \approx 300\,000$. It has been reported (Ward-Smith 1980) that axial separation is always observed in curved tubes with a/R less than about 1.5, but this occurs for very large values of Re (order 10^4 or larger).

There have also been a number of studies of developing flow in a duct of square or rectangular cross-section. Axial flow separation is known to occur in the outer corners of such ducts (Chung & Hyun 1992; Humphrey, Taylor & Whitelaw 1977; Soh 1988). However, this separation is not analogous to that seen in the present study, since it occurs by a different mechanism not related to secondary flow effects *per se*, and since it occurs on the outer wall (corresponding to the bed in our geometry). Axial flow separation on the inner wall was not observed in these studies, which considered Dean numbers up to 933. On the other hand, Shiragami & Inoue (1986) observed axial flow separation in their experimental studies of flow in a 90° bend in a rectangular duct. However, they attached their bend to a long straight upstream duct section to produce fully developed flow entering the bend. Additionally, flow was likely to be turbulent for larger Dean numbers. Therefore, their inlet conditions differed from those expected for entry flow from a reservoir. They reported critical Dean numbers for separation ranging from 2000 to 3000, depending on curvature ratio. The structure of their separation region is not described in detail, but is consistent with a model based on secondary flow collision on the symmetry plane.

4.1.2. *Mechanics of separation in the junction geometry*

There is an important difference between flow in the junction and the majority of the above-cited studies. Specifically, in our work, the flow approaching the toe is Poiseuille, and is thus not analogous to entry flow from a reservoir. This has two important implications.

The concept of an axial flow boundary layer is no longer valid. However, the idea of a secondary flow boundary layer is still conceptually useful (note the large concentration of vorticity in the near-wall regions just distal to the toe; figure 23). Therefore, despite the lack of an irrotational core flow in the junction geometry, we can speak of a secondary flow collision that has qualitative similarities to the theory put forward by Stewartson *et al.* (1980).

A Poiseuille inlet flow favours separation more than an inviscid inlet profile (Olsen & Snyder 1985). This difference is due to two reasons. First, the lower-wall shear rate in Poiseuille flow is easier to reverse (for a given pressure gradient) than that in a developing inviscid flow. Second, a potential vortex core forms when flow enters from a reservoir; this vortex shifts the velocity peak towards the inner wall, at least for stations close to the bend inlet, and therefore increases inner-wall axial shear.

Additionally, the Dean number for the junction geometry is not well-defined, thereby complicating direct comparison with studies in curved tubes and ducts. As a rough estimate of an effective Dean number in our study, we note that at $Re_D = 550$ the maximum secondary velocity occurs just downstream of the toe, and is equal to 112% of the mean inlet velocity. This can be compared with maximum secondary velocities of 87% of the mean inlet velocity data for entry flow in a duct with $\kappa = 368$ (Soh 1988) and 45% for entry flow in a tube with $\kappa = 679$ (Agrawal *et al.* 1978). Although secondary velocities depend both on κ and curvature ratio for large κ, the above comparison suggests that the effective Dean number in the junction geometry is at least 700.

Despite these differences, a secondary flow collision model best explains the separation events in the junction geometry, as follows. Consider first the separation zone just distal to the toe at $Re_D = 550$. It is noteworthy that both computations and experiments show flow separation about 0.1 diameters distal to the toe, and not at the toe as might first be expected. This implies that the transverse pressure gradient is sufficiently strong to keep the flow attached at the toe, at least for the Reynolds numbers considered in this work, and that separation is not due to the inability of the fluid to negotiate the corner at the toe. Instead, separation is triggered due to a secondary flow collision effect downstream of the toe. This collision can be thought of as being centred at a free stagnation point, which for $Re = 550$ occurs at $Z = 0.80$, $Y = -0.85$ (figure 8*c*; see also nodes adjacent to lower wall in figure 18*b*). The elevated pressure associated with this stagnation point creates an unfavourable axial pressure gradient for fluid near the host-tube wall at $Z < 0.80$, which (for $Re_D > 200$) causes axial flow separation proximal to the free stagnation point. This separation leads to the displacement of the primary axial flow away from the lower wall, as evident in figure 8(*b*). Associated with this free stagnation point, there is a favourable near-wall pressure gradient for $Z > 0.80$, which causes fluid being supplied by the secondary flow boundary layer to turn distally and re-establish distally directed flow.

For Reynolds numbers greater than about 450, the secondary flow is strong enough for this entire process to repeat itself at about 1.5 diameters distal to the toe, leading to a second separation event.† As the Reynolds number increases beyond 450, the secondary flows increase in intensity relative to the axial flow, tightening the helical path of the high-momentum fluid in the host tube. This causes the proximal edge of

† In view of the above scenario, one could even imagine a third separation event occurring along the lower wall at high enough Reynolds number. We did not see any evidence for this in our study, no doubt due to the fact that the secondary flow is significantly attenuated by viscous effects for $Z > 2.0$. However, close inspection of figure 108 of Nakayama, Woods & Clark (1988) shows just such a third separation event for flow at $Re = 2000$ in a pipe elbow.

the second retrograde flow zone to move towards the toe. However, the second zone is prevented from growing too far in this direction by fluid travelling distally from the first retrograde flow zone. Therefore, for $Re_D > 600$, growth of the second retrograde flow zone occurs via the development of 'legs' that extend proximally and laterally from the main body of the retrograde flow zone (figure 19). The focal point on these legs is associated with the generation of a large amount of r-vorticity, as discussed above.

The flow structure in the neighbourhood of the free stagnation point(s) in this flow is particularly interesting. Immediately adjacent to the lower wall is a region of secondary flow separation, i.e. secondary flow moving away from the symmetry plane. This is overlain by a region characterized by non-separated secondary flow, in which the free stagnation point is embedded. This in turn is overlain by a region of axially moving fluid. This three-layer structure is very similar to that proposed by Stewartson & Simpson (1982), although of course they were working within the context of a boundary layer analysis.

At a lower Re_D of 400, a boundary layer collision again leads to axial flow separation. However, the strength of the secondary flows is somewhat less, so that there is no secondary flow separation at $Z \approx 0.7$ (figure 20a). Instead, the secondary flow collision occurs on the lower wall of the host tube, giving rise to a half-node on the symmetry plane of the model (figure 18a). Fluid that collides on the symmetry plane leaves the surface of the lower wall, flowing distally and proximally along the lower wall from the collision point (figure 18a). Thus, the flow has a simpler two-layer structure in the neighbourhood of this point: an attached secondary flow impinges on the symmetry plane, displacing the axial flow away from the lower wall and leading to axial flow separation. This interesting flow structure does not seem to have been explicitly predicted by Stewartson & Simpson (1982). It depends critically on having just the right magnitude of secondary flows, i.e. strong enough to allow a secondary flow collision on the symmetry plane, but not so strong as to induce secondary flow separation in the collision region. Once the Reynolds number increases sufficiently to induce secondary flow separation, the collision point moves off the lower wall of the host tube and the three-layer structure discussed above is obtained.

4.2. *Comments on the accuracy of the results*

There are a number of factors that affect the accuracy of the numerical calculations and the experimental data. Computationally, the factor that had the most significant effect on the results was mesh density, especially for wall shear stresses, thus necessitating very highly refined meshes. Other factors, such as the stopping criterion for the calculation, the time step, and the stopping criterion for the iterative solvers were carefully tested to ensure that they did not change the computed results. The sensitive dependence of wall shear stress patterns on mesh density is consistent with other observations (e.g. see figure 8 of Humphrey *et al.* (1985) and figure 4 of Tutty & Pedley (1993)). Experimentally, the major uncertainty occurred in positioning the model with respect to the laser beam, which may have caused the actual measurement planes to differ slightly from their nominal locations. Positioning errors, particularly on measurement planes away from the $Y = 0$ or $X = 0$ planes, interact with refractive index difference between the model and the working fluid to cause further uncertainty in the trace position. There was also evidence of weak asymmetry in the experimentally measured flow field, as can be seen by comparing figure 13(a) with 13(c).

Despite these errors, the agreement between computed and experimentally measured

velocities is generally very good – ranging from excellent on the symmetry plane (figure 12) to good on other planes (figures 13 and 14). However, the agreement in wall shear stresses (figures 16 and 17) is much less satisfactory, which we believe is due to several effects. First, wall shear stress is very difficult to measure experimentally, and thus there is expected to be uncertainty in this measured quantity. Second, the experimental flow field suffered from some asymmetry, which must have affected the wall shear stress data. Third, the wall shear stress measurements were taken at a different time than the velocity measurement, and thus may have been subject to a different set of model alignment errors than was the case for the velocity measurements. In this regard, it is important to note that the error bars observed in figures 16 and 17 are based on standard errors of the mean for multiple measurements with the model in the same position. Thus, these error bars represent the repeatability of that set of measurements, but do not incorporate effects such as flow field asymmetry and model misalignment. They must therefore be regarded as lower bounds on the total measurement error of wall shear stress. Fourth, in the finite element simulations, the 'toe' of the junction was modelled as 'sharp' (i.e. with a slope discontinuity). This region is therefore singular in the finite element context, which could have possibly introduced local effects that affected, for example, the length of the first recirculation zone.

Despite these uncertainties in the experimentally measured wall shear stress, the major physical features of the flow were entirely consistent between the numerical and experimental measurements. This certainly enhances confidence in our results. Further, because of the well-validated nature of the numerical code and the systematic adaptive mesh refinement studies, we believe that the computed wall shear stress features are quantitatively correct.

4.3. *Pulsatile flow effects*

The original impetus of this work was the examination of blood flow dynamics in the arterial system, where flow is pulsatile. It would therefore be of interest to extend the present study to consider unsteady conditions. Chandran and Yearwood (Chandran & Yearwood 1981; Yearwood & Chandran 1984) studied pulsatile flow in a curved tube, with application to flow in the human aortic arch. They observed strong temporal variations of secondary flows, as well as strong retrograde flows along the inner wall during diastole (decelerating and minimum flow phase). Extrapolating these observations to the present case suggests that the separation regions that we observed under steady flow would be created during systole (peak flow phase) and would then possibly collapse (by an unknown mechanism) during diastole. Particularly interesting in this context would be examination of the dynamic behaviour of singular points in the wall shear stress field. For example, foci are points where blood cells in the vicinity of the wall, such as platelets and macrophages, may tend to accumulate, thereby increasing their exposure time to endothelial cells lining the artery wall.

The pulsatile flow situation is further complicated by other effects. For example, 'vortex waves' have been observed in two-dimensional or quasi-two-dimensional flows both experimentally (Sobey 1985) and computationally (Tutty 1992; Tutty & Pedley 1993). Tutty & Pedley (1993) observed the formation of strong vortices in a two-dimensional channel, caused by the roll-up of vorticity shed from the channel walls. The interaction between this shed vorticity and a separation region downstream of a step was central to the initiation of these vortices, which in turn markedly affected the wall shear stress distribution. Whether such effects would occur in an unsteady flow containing fully three-dimensional separation patterns is an open question.

Examination of this and other pulsatile flow effects would be worthwhile, although in view of the high mesh densities needed in the present study, it would require a significant investment in computational resources.

4.4. *Summary*

Flow in a model end-to-side anastomosis demonstrates axial flow separation driven by a secondary boundary layer collision, analogous to that originally predicted for entry flow in a curved tube. The strong secondary flows in the present geometry cause axial separation to occur at Reynolds numbers of order several hundred, despite the fact that an analogous separation event does not occur in curved tubes at a comparable *Re*. For $Re \geqslant 400$, two separation zones form and interact, each of which is driven by a secondary boundary layer collision.

This work was supported by the Natural Sciences and Engineering Research Council of Canada through the Collaborative Grants Program and an EWR Steacie Fellowship (CRE), by the Heart and Stroke Foundation of Ontario and the Medical Research Council of Canada (MO). We are grateful to Dr C. Lorencez for his patience in digitizing some of the photographs.

REFERENCES

Agrawal, Y., Talbot, L. & Gong, K. 1978 Laser anemometer study of flow development in curved circular pipes. *J. Fluid Mech.* **85**, 497–518.

Armaly, B. F., Durst, F., Periera, J. C. & Schonung, B. 1983 Experimental and theoretical investigation of backward-facing step flow. *J. Fluid Mech.* **127**, 473–496.

Berger, S. A., Talbot, L. & Yao, L. S. 1983 Flow in curved pipes. *Ann. Rev. Fluid Mech.* **15**, 461–512.

Bovendeerd, P. H., Steenhoven, A. A. van, Vosse, F. N. van de & Vossers, G. 1987 Steady entry flow in curved pipes. *J. Fluid Mech.* **177**, 233–246.

Cahouet, J. & Chabard, J. 1988 Some fast 3D finite element solvers for the generalized Stokes problem. *Intl J. Numer. Meth. Fluids* **8**, 869–895.

Chandran, K. B. & Yearwood, T. L. 1981 Experimental study of physiological pulsatile flow in a curved tube. *J. Fluid Mech.* **111**, 59–85.

Choi, U. S., Talbot, L. & Cornet, I. 1979 Experimental study of wall shear rates in the entry region of a curved tube. *J. Fluid Mech.* **93**, 465–489.

Chung, J. H. & Hyun, J. M. 1992 Convective heat transfer in the developing flow region of a square duct with strong curvature. *Intl J. Heat Mass Transfer* **35**, 2537–2550.

Couch, G. G., Johnston, K. W. & Ojha, M. 1996 Full-field flow visualization and velocity measurement with a photochromic grid method. *Measurement Sci. Tech.* **7**, 1238–1246.

Couch, G. G., Kim, H. & Ojha, M. 1997 *In vitro* assessment of the hemodynamic effects of a partial occlusion in a vena cava filter. *J. Vascular Surgery* **25**, 663–672.

Ethier, C. R. & Steinman, D. A. 1994 Exact fully 3D Navier–Stokes solutions for benchmarking. *Intl J. Numer. Meth. Fluids* **19**, 369–375.

Ethier, C. R., Steinman, D. A. & Ojha, M. 1999 Comparisons between computational hemodynamics, photochromic dye flow visualization and magnetic resonance velocimetry. In *Hemodynamics of Internal Organs* (ed. M. W. Collins & Y. Xu). Computational Mechanics Publications.

Glowinski, R. & Pironneau, O. 1992 Finite element methods for Navier–Stokes equations. *Ann. Rev. Fluid Mech.* **24**, 167–204.

Henk, R. W. & Reed, H. L. 1993 The analysis of unsteady three-dimensional flow separation. *AIAA Paper* 93-0642.

Humphrey, J. A., Iacovides, H. & Launder, B. E. 1985 Some numerical experiments on developing laminar flow in circular-sectioned bends. *J. Fluid Mech.* **154**, 357–375.

Humphrey, J. A., Taylor, A. M. & Whitelaw, J. H. 1977 Laminar flow in a square duct of strong curvature. *J. Fluid Mech.* **83**, 509–527.

Hunt, J. C., Abell, C. J., Peterka, J. A. & Woo, H. 1978 Kinematical studies of the flows around free or surface-mounted obstacles; applying topology to flow visualization. *J. Fluid Mech.* **86**, 179–200.

Iribarne, A., Frantisak, F., Hummel, R. L. & Smith, J. W. 1972 An experimental study of instabilities and other flow properties of a laminar pipe jet. *AIChEJ.* **18**, 689–698.

Ito, H. 1987 Flow in curved pipes. *JSME Intl J.* **30**, 543–552.

Keast, P. 1986 Moderate-degree tetrahedral quadrature formulas. *Comput. Meth. Appl. Mech. Engng* **55**, 339–348.

Kluwick, A. & Wohlfart, H. 1984 Entry flow in weakly curved ducts. *Ingenieur-Archiv* **54**, 107–120.

Kluwick, A. & Wohlfart, H. 1986 Hot-wire-anemometer study of the entry flow in a curved duct. *J. Fluid Mech.* **165**, 335–353.

Liu, A. & Joe, B. 1996 Quality local refinement of tetrahedral meshes based on 8-subtetrahedron subdivision. *Maths Comput.* **65**, 1183–1200.

Liu, S. & Masliyah, J. H. 1996 Steady developing laminar flow in helical pipes with finite pitch. *Comput. Fluid Dyn.* **6**, 209–224.

Macagno, E. O. & Hung, T. K. 1967 Computational and experimental study of a captive annular eddy. *J. Fluid Mech.* **28**, 43–64.

Maday, Y., Patera, A. T. & Rønquist, E. M. 1990 An operator-integration-factor splitting method for time-dependent problems: application to incompressible fluid flow. *J. Sci. Comput.* **5**, 263–292.

Minev, P. D. & Ethier, C. R. 1998 A characteristic/finite element algorithm for the Navier-Stokes equations using unstructured grids. *Comput. Meth. Appl. Mech. Engng* **178**, 39–50.

Nakayama, Y., Woods, W. A. & Clark, D. G. (Eds.) 1988 *Visualized Flow. Fluid Motion in Basic and Engineering Situations Revealed by Flow Visualization.* Japan Society of Mechanical Engineers. Pergamon.

Nerem, R. M. & Cornhill, J. F. 1980 The role of fluid mechanics in atherogenesis. *ASME J. Biomech. Engng* **102**, 181–189.

Ojha, M. 1993 Spatial and temporal variations of the wall shear stress within an end-to-side arterial anastomosis model. *J. Biomech.* **26**, 1377–1388.

Ojha, M. 1995 Flow separation and the transition to unsteadiness. In *Proc. 1995 Bioengineering Conf.* (ed. R. M. Houchmuth). ASME BED, vol. 29.

Ojha, M., Cobbold, R. S. C., Johnston, K. W. & Hummel, R. L. 1989 Pulsatile flow through constricted tubes: an experimental investigation using photochromic tracer methods. *J. Fluid Mech.* **203**, 173–197.

Ojha, M., Cobbold, R. S., Johnston, K. W. & Hummel, R. L. 1990 Detailed visualization of pulsatile flow fields produced by modelled arterial stenoses. *J. Biomed. Engng* **12**, 463–469.

Ojha, M., Hummel, R. L., Cobbold, R. S. & Johnston, K. W. 1988 Development and evaluation of a high resolution photochromic dye method for pulsatile flow studies. *J. Phys.* E: *Sci. Instrum.* **21**, 998–1004.

Olsen, D. E. & Snyder, D. 1985 The upstream scale of flow development in curved circular pipes. *J. Fluid Mech.* **150**, 139–158.

Pauley, L. A. 1994 Structure of local pressure-driven three-dimensional transient boundary layer separation. *AIAA J.* **31**, 997–1005.

Pauley, L. A., Moin, P. & Reynolds, W. C. 1990 The structure of two-dimensional separation. *J. Fluid Mech.* **220**, 397–411.

Prakash, S. 1999 Adaptive mesh refinement for finite element flow modeling in complex geometries. PhD thesis, Department of Mechanical and Industrial Engineering, University of Toronto.

Prakash, S. & Ethier, C. R. 1999 Enhanced error estimator for adaptive finite element analysis of 3D incompressible flow. *Comput. Meth. Appl. Mech. Engng* (Submitted).

Prakash, S. & Ethier, C. R. 2000 An h-adaptive technique for finite element analysis of flow in complex 3D geometries. (In preparation.)

Shiragami, N. & Inoue, I. 1986 Pressure losses in rectangular bends. In *Encyclopedia of Fluid Mechanics*, Vol. 1 (ed. N. P. Cheremisinoff), Chap. 26. Gulf.

Sobey, I. J. 1985 Observation of waves during oscillatory channel flow. *J. Fluid Mech.* **151**, 395–426.

Soh, W. Y. 1988 Developing fluid flow in a curved duct of square cross-section and its fully developed dual solutions. *J. Fluid Mech.* **188**, 337–361.

Soh, W. Y. & Berger, S. A. 1984 Laminar entrance flow in a curved pipe. *J. Fluid Mech.* **148**, 109–135.

Steinman, D. A., Frayne, R., Zhang, X. D., Rutt, B. K. & Ethier, C. R. 1996 MR measurement and numerical simulation of flow in an end-to-side anastomosis model. *J. Biomech.* **29**, 537–542.

Stewartson, K., Cebeci, T. & Chang, K. C. 1980 A boundary-layer collision in a curved duct. *Q. J. Mech. Appl. Maths* **33**, 59–75.

Stewartson, K. & Simpson, C. J. 1982 On a singularity initiating a boundary-layer collision. *Q. J. Mech. Appl. Maths* **35**, 1–16.

Talbot, L. & Wong, S. J. 1982 A note on boundary layer collision in a curved pipe. *J. Fluid Mech.* **122**, 505–510.

Tananayev, A. V., Gontsov, N. G. & Marinova, O. A. 1982 Flow structure in pipe elbows. *Fluid Mech. – Sov. Res.* **11**, 7–13.

Tanishita, K., Suzuki, J., Ohishi, N. & Naruse, T. 1991 Steady entrance flow in a strongly curved tube. *Nippon Kikai Gakkai Ronbunshu, B Hen* **57**, 898–904.

Tobak, M. & Peake, D. J. 1982 Topology of three-dimensional separated flows. *Ann. Rev. Fluid Mech.* **14**, 61–85.

Tutty, O. R. 1992 Pulsatile flow in a constricted channel. *ASME J. Biomech. Engng* **114**, 50–54.

Tutty, O. R. & Pedley, T. J. 1993 Oscillatory flow in a stepped channel. *J. Fluid Mech.* **247**, 179–204.

Vosse, F. N. van de, Steenhoven, A. A., Segal, A. & Janssen, J. D. 1989 A finite element analysis of the steady laminar entrance flow in a 90° curved tube. *Intl J. Numer. Meth. Fluids* **9**, 275–287.

Ward-Smith, A. J. 1980 *Internal Fluid Flow: The Fluid Dynamics of Flow in Pipes and Ducts.* Clarendon.

Yao, L. S. & Berger, S. A. 1988 The three-dimensional boundary layer in the entry region of curved pipes with finite curvature ratio. *Phys. Fluids* **31**, 486–494.

Yearwood, T. L. & Chandran, K. B. 1984 Physiological pulsatile flow experiments in a model of the human aortic arch. *J. Biomech.* **15**, 683–704.

Zienkiewicz, O. C. & Zhu, J. Z. 1992 The superconvergent patch recovery and a posteriori error estimates. Part 1: The recovery technique. *Intl J. Numer. Meth. Engng* **33**, 1331–1364.